



Norwegian University of
Science and Technology

Numerical Study of Radiation Hazard from Advanced Flare Systems at Process Plants

Marthe Hove Bjørnæs

Master of Science in Mechanical Engineering

Submission date: June 2016

Supervisor: Terese Løvås, EPT

Co-supervisor: Morten Stenstad Lien, Lilleaker Consulting AS

Norwegian University of Science and Technology
Department of Energy and Process Engineering

EPT-M-2016-16

MASTEROPPGAVE

for

Student

Marthe Hove Bjørnæs

Våren 2016

Numerisk studie av strålingsfare fra avanserte fakkelsystem ved prosessanlegg*Numerical study of radiation hazard from advanced flare systems at process plants***Bakgrunn og målsetting**

Kontinuerlig fakling eller trykkavlastning gjennom antent fakkell ved nødavstengning av et prosessanlegg kan medføre uakseptable strålingsverdier mot utstyr og personell på dekk hvis ikke dette er tilstrekkelig designet for. Valg av fakkeltipe og høyde på fakkeltårnet er derfor essensielt for å unngå dette. Dette forutsetter gode modeller for beregning av stråling. Gode, validerte analytiske/empiriske modeller eksisterer for rørfakler med ett utslipprør, men modellene er ikke funnet like presise for utslipp fra mer avanserte fakkelsystem, spesielt ved lavere utslippsrater enn fakkelsystemet er optimalisert for.

CFD-beregninger kan brukes til å vurdere stråling fra mer avanserte fakkeltyper, og kan i tillegg være spesielt gunstig for å vurdere for eksempel strålingsskjerming av utstyr. En stor utfordring er imidlertid avveiningen mellom høy nok oppløsning på beregninger og akseptabel simuleringstid. Høyden på fakkeltårnet til dekk/utstyr/struktur som man ønsker å evaluere stråling på gir i seg selv behov for et stort beregningsdomene, gridcellene kan ikke være for store på dekk for å få representert geometrien tilfredsstillende, samtidig må man regne med at dysene, spredning av gass og stråling fra fakkell i seg selv krever høy oppløsning. Valg av oppløsning vil dermed påvirke nøyaktigheten av det endelige resultatet, men i hvor stor grad er ofte problematisk å verifisere. Videre er valg av passende submodeller i slike CFD verktøy viktig, samt korrekte initialbetingelser for simuleringen.

Temaet i denne oppgaven er strålingsfare for eksponert utstyr på dekk og tilhørende strukturer, og hensikten/målet er å finne hvordan utslipp fra et avansert fakkelsystem kan modelleres i det numeriske beregningsverktøyet KFX på en optimal måte. Strålingsdata fra et system med en høytrykksfakkell og en lavtrykksfakkell med tilhørende omgivelsesforhold finnes tilgjengelig i en slik detaljgrad at scenariet kan gjenskapes i KFX, og det vil søkes å sammenlikne simuleringresultatene opp mot disse målingene.

Dette er en videreføring av prosjektoppgaven høsten 2015 innen samme tema. Mens prosjektoppgaven så på enkle rørfakler, vil masteroppgaven ta for seg mer avanserte fakkelsystemer.

Oppgaven bearbeides ut fra følgende punkter

- 1) Nødvendig bakgrunnsstudie om fakkelsystemer og bruk av mer avanserte fakkelsystemer, samt sette seg inn i utfordringer relatert til dagens standard angående stråling fra fakler.
- 2) Definere og sette opp et passende fakkelsystem for å utføre en gridsensitivitetsanalyse. Dette innebærer valg av grensebetingelser, submodeller (stråling, gassammensetning etc)
- 3) Definere og sette opp et passende system for å studere strålingsparametere i modellene. Dette kan være samme som i 2), eller et forenklet system der det finnes tilgjengelig måledata.
- 4) Gjøre numeriske beregninger som blir grunnlag for endelig komparativ studie.

Senest 14 dager etter utlevering av oppgaven skal kandidaten levere/sendte instituttet en detaljert fremdrift- og eventuelt forsøksplan for oppgaven til evaluering og eventuelt diskusjon med faglig ansvarlig/veiledere. Detaljer ved eventuell utførelse av dataprogrammer skal avtales nærmere i samråd med faglig ansvarlig.

Besvarelsen redigeres mest mulig som en forskningsrapport med et sammendrag både på norsk og engelsk, konklusjon, litteraturliste, innholdsfortegnelse etc. Ved utarbeidelsen av teksten skal kandidaten legge vekt på å gjøre teksten oversiktlig og velskrevet. Med henblikk på lesning av besvarelsen er det viktig at de nødvendige henvisninger for korresponderende steder i tekst, tabeller og figurer anføres på begge steder. Ved bedømmelsen legges det stor vekt på at resultatene er grundig bearbeidet, at de oppstilles tabellarisk og/eller grafisk på en oversiktlig måte, og at de er diskutert utførlig.

Alle benyttede kilder, også muntlige opplysninger, skal oppgis på fullstendig måte. For tidsskrifter og bøker oppgis forfatter, tittel, årgang, sidetall og eventuelt figurnummer.

Det forutsettes at kandidaten tar initiativ til og holder nødvendig kontakt med faglærer og veileder(e). Kandidaten skal rette seg etter de reglementer og retningslinjer som gjelder ved alle (andre) fagmiljøer som kandidaten har kontakt med gjennom sin utførelse av oppgaven, samt etter eventuelle pålegg fra Institutt for energi- og prosesssteknikk.

Risikovurdering av kandidatens arbeid skal gjennomføres i henhold til instituttets prosedyrer. Risikovurderingen skal dokumenteres og inngå som del av besvarelsen. Hendelser relatert til kandidatens arbeid med uheldig innvirkning på helse, miljø eller sikkerhet, skal dokumenteres og inngå som en del av besvarelsen. Hvis dokumentasjonen på risikovurderingen utgjør veldig mange sider, leveres den fulle versjonen elektronisk til veileder og et utdrag inkluderes i besvarelsen.

I henhold til ”Utfyllende regler til studieforskriften for teknologistudiet/sivilingeniørstudiet” ved NTNU § 20, forbeholder instituttet seg retten til å benytte alle resultater og data til undervisnings- og forskningsformål, samt til fremtidige publikasjoner.

Besvarelsen leveres digitalt i DAIM. Et faglig sammendrag med oppgavens tittel, kandidatens navn, veileders navn, årstall, institutt navn, og NTNUs logo og navn, leveres til instituttet som en separat pdf-fil. Etter avtale leveres besvarelse og evt. annet materiale til veileder i digitalt format.

- Arbeid i laboratorium (vannkraftlaboratoriet, strømningssteknisk, varmeteknisk)
 Feltarbeid

NTNU, Institutt for energi- og prosesssteknikk, 13. januar 2015



Olav Bolland
Instituttleder



Terese Løvås
Faglig ansvarlig/veileder

Medveileder(e): Morten Stenstad Lien, Lilleaker Consulting AS

Preface

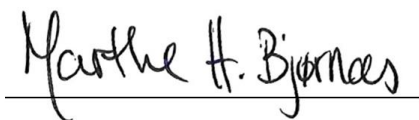
This master thesis is the closing chapter of my five years as a student at NTNU, studying under the department of Energy and Process Engineering. My last year has been spent together with Lilleaker Consulting AS in Sandvika, where the thesis has been carried out. I am very grateful for the facilitation Lilleaker has provided me to make this thesis possible, especially Tor Gulbrandsen who initiated the collaboration. I have gained valuable knowledge both academically and generally in life this last year, being surrounded by these competent people. A special thanks goes to Morten Stenstad Lien who has been my supervisor at Lilleaker. His guidance, support and sense of humor have been invaluable and sharing the frustration when KFX decides to not cooperate has been appreciated.

I would also like to thank my supervisor at NTNU, Terese Løvås, for giving me encouraging feedback throughout the process and always be available on my occasional trips to Trondheim.

This thesis would not be half as meaningful without the measurements from a real flaring scenario provided by SINTEF Energiforskning AS. A thanks goes to Øyvind Langørgen for arranging access to these data.

One final thanks goes to my family. Their unlimited support has been of great importance.

Sandvika, June 2016

A handwritten signature in black ink, reading "Marthe H. Bjørnæs", written over a horizontal line.

Marthe Hove Bjørnæs

Abstract

This thesis investigates how to optimize the calculation of thermal radiation from an advanced flare system in the numerical computation tool Kameleon FireEx (KFX). Measured radiation levels from a real flaring scenario at an offshore installation are used as reference. The flare system consists of one high pressure flare and one low pressure flare.

An optimal approach for calculating radiation levels implies a trade-off between accuracy of the solution and numerical simulation time. To obtain a high degree of accuracy the size of the release cells and the nearby cells must be sufficiently small to capture the large gradients close to the release. This makes requirements of how the release cells should be defined and different configurations have been tried. The first cases were simulated using only one release cell for each flare which gives a low resolution. The resolution has then been refined by dividing the release cells into multiple smaller cells.

There is a clear connection between the refinement of the release cells and the accuracy of the calculated radiation levels. The smaller cells are used, the greater agreement there is between simulated and measured radiation levels. Smaller cells lead to longer simulation time but this can be reduced by removing cells other places in the calculation domain. As the process equipment usually existing on the platform deck is removed in this specific scenario as a simplification, this allows for larger cell sizes far away from the flares.

The conclusion of this study is that using 9 release cells for the high pressure flare together with 4 release cells for the low pressure flare was the most optimal approach for the scenario simulated in this thesis. It was in this case very low deviation between simulated and measured radiation levels, and the simulation time was considered acceptable. This configuration might not be the most optimal for any given flare; therefore sensitivity tests regarding release cell size should be conducted for other scenarios. The general conclusion is nevertheless that a high resolution of the release cells will give more accurate radiation levels.

Sammendrag

Denne avhandlingen undersøker hvordan man kan optimalisere beregningen av termisk stråling fra et avansert fakkelsystem i det numeriske beregningsverktøyet Kameleon FireEx (KFX). Målte strålingsnivåer fra et reelt faklingsscenario på en offshoreinstallasjon benyttes som sammenligningsgrunnlag. Fakkelsystemet består av en høytrykksfakkell og en lavtrykksfakkell.

En optimal metode for å beregne ståling innebærer en avveining mellom nøyaktighet på resultatene og den numeriske regnetiden. For å oppnå høy grad av nøyaktighet må størrelsen på utslippscellene og de omkringliggende cellene være liten nok til å fange opp de store gradientene nærme utslippet. Dette stiller krav til hvordan utslippscellene defineres, og ulike oppsett er testet ut. De første casene ble simulert med kun én utslippscelle per fakkell noe som gir en lav oppløsning. Oppløsningen har så blitt forfinet ved å dele utslippscellene inn i flere mindre celler.

Det er en klar sammenheng mellom oppløsningen på utslippscellene og nøyaktigheten på strålingsnivåene som beregnes. Jo flere mindre celler som brukes, jo større samsvar er det mellom simulerte og målte strålingsnivåer. Mindre utslippsceller fører til lengre regnetid, men denne kan igjen kortes ned ved å fjerne celler andre steder i beregningsdomenet. Da prosessutstyr som vanligvis ville fantes på dekk er fjernet i dette spesifikke scenarioet som en forenkling åpner dette opp for å ha store cellestørrelser langt unna faklene.

Konklusjonen av studien er at 9 utslippsceller for høytrykksfakkelen sammen med 4 celler for lavtrykksfakkelen var det mest optimale oppsettet i scenariet simulert i denne avhandlingen. Det var da svært lavt avvik mellom simulerte og målte strålingsverdier, samtidig med at regnetiden ble ansett som akseptabel. Generelt vil man ikke kunne si at dette oppsettet er mest optimalt uansett fakkell, så en sensitivitetstest i forhold til valg av størrelse på utslippscellene bør gjennomføres for andre scenarier. Den generelle konklusjonen er allikevel at høyere oppløsning på utslippscellene vil gi mer nøyaktige strålingsnivåer.

Contents

Preface	i
Abstract	iii
Sammendrag	v
Contents	vii
Nomenclature	ix
List of Figures	xi
List of Tables	xiii
1 Introduction	1
2 Background	3
2.1 Flare Types	3
2.2 Thermal Radiation	4
2.3 Parameters Affecting the Radiation Level	6
2.4 Thermal Radiation Modeling Techniques	6
3 KFX	11
3.1 Numerics in KFX	11
3.2 Equivalent Jet Exit	15
3.3 Release Cells	17
3.4 The Radiation Model in KFX	25
4 Simulations	33
4.1 The Flare System	33
4.2 Geometry and Measuring Points	34
4.3 Parameter Values	36
4.4 Case Setup	39
5 Results	45
5.1 Flare Flames	45
5.2 Radiation Levels	48
5.3 Simulation Time	52
5.4 Discussion	55
6 Conclusion	57
6.1 Further Work	57
References	59
Appendix A Sensitivity Tests	A-1
A.1 Restart Files	A-1
A.2 Courant Number	A-4
A.3 Number of Ordinates	A-5

Nomenclature

Latin symbols

a, b	Coefficients (discretization)	
A	Area	m^2
c	Local speed of sound	m/s
C	Courant number	
D	Distance	m
d_e	Diameter of equivalent jet exit	m
d_j	Diameter of flare tip exit	m
E	Emissive power	W/m^2
h	Enthalpy	J/kg
I	Radiation intensity	W/m^2sr
I_-	Incident intensity	W/m^2sr
I_+	Outgoing intensity	W/m^2sr
J	Flux	kg/s
L	CV length or Monin-Obukhov length	m
L_k	Ray path length	m
\dot{m}_j	Mass rate of fuel gas	kg/s
M	Mach number	
M_∞	Molecular mass of air	$kg/kmol$
M_j	Molecular mass of fuel gas	$kg/kmol$
\mathbf{n}	Normal unit vector	
p	Pressure	N/m^2
Q	Heat release	W
\mathbf{q}	Heat flux (convective, diffusive or radiative)	W/m^2
q_-	Incident radiative heat flux	W/m^2
q_+	Outgoing radiative heat flux	W/m^2
\mathbf{r}	Ray position vector	m
R_H	Relative humidity of ambient air	$\%$
S_ϕ	Source term for quantity ϕ	
\mathbf{s}_k	Ray direction	
t	Time	s
T_j	Temperature of fuel gas	$^\circ C$ or K
T_s	Temperature of a surface	$^\circ C$ or K
U	Velocity	m/s
U_*	Friction velocity	m/s
U_∞	Wind velocity	m/s
u, v, w	Velocity components in x-, y- and z-direction	m/s
V	Volume	m^3
Z_0	Surface roughness length	m

Greek symbols

α	Angle	°
ε_s	Surface emissivity	
Γ_ϕ	Diffusion coefficient of quantity ϕ	
κ	Absorption coefficient or von Karman's constant	
Ω	Solid angle	sr
ϕ	General quantity or azimuthal angle	
$\Phi(\mathbf{s}_i, \mathbf{s})$	Scattering phase function	
ρ	Density	kg/m ³
σ	Stefan-Boltzmann's constant	W/m ² K ⁴
σ_s	Scattering coefficient	1/m
τ	Transmissivity factor	
τ_w	Wall shear stress	kg/ms ²
θ	Polar angle	rad

Sub- and superscripts

*	Guessed value (in SIMPLEC algorithm)
°	Conditions after previous time step (discretization)
i, j, k	Tensor notation; = 1, 2 or 3 representing x, y and z
n, s, e, w, t, b	North, south, east, west, top and bottom (grid)

Abbreviations

API	American Petroleum Institute
CV	Control Volume
ComputIT	Computational Industry Technologies AS
FVM	Finite Volume Method
HP	High Pressure
KFX	Kameleon FireEx
LHV	Lower Heating Value
LP	Low Pressure
NORSOK	Norsk Søkkel Konkurransesjjon
SIMPLEC	Semi Implicit Method for Pressure Linked Equations Consistent

List of Figures

Figure 2.1: Pipe-flare tip (Prema-Service)	3
Figure 2.2: Multiple nozzle flare tips (Prema-Service).....	4
Figure 2.3: Electromagnetic spectrum (J. White & Bussman, 2012, fig. 8.1)	4
Figure 2.4: Empirical modeling approaches (J. White & Bussman, 2012, fig. 8.12)	7
Figure 3.1: Staggered grid in two dimensions (Versteeg & Malalasekera, 2007, fig. 6.5).....	12
Figure 3.2: Scalar control volume, u-control volume and v-control volume (Thermal- FluidsCentral, 2010).....	12
Figure 3.3: Flowchart of the SIMPLEC algorithm (Versteeg & Malalasekera, 2007, fig. 6.6 and 8.10).....	14
Figure 3.4: Schematic of shock structure (B.E. Vembe et al., 2001, fig. 4.6)	16
Figure 3.5: Calculation model for the equivalent jet exit (B.E. Vembe et al., 2001, fig. 4.7) .	17
Figure 3.6: Release cell: control volume representing the fuel discharge	18
Figure 3.7: Illustration of converting the area of the circular jet exit to a CV cell	19
Figure 3.8: Decomposition of release velocity at an inclined flare tip	20
Figure 3.9: Fixed areas at release cells for inclined releases	21
Figure 3.10: Release cell subdivision used in the release cell sensitivity test	23
Figure 3.11: Radiation levels from release cell sensitivity test.....	24
Figure 3.12: Control volume influenced by radiation (Versteeg & Malalasekera, 2007, fig. 13.3).....	26
Figure 3.13: Angular notation for equation (3.21) and (3.22). Incoming intensity is used as example (Versteeg & Malalasekera, 2007, fig. 13.4).....	27
Figure 3.14: Schematic of a ray in a medium with absorptive, emissive and scattering properties (Versteeg & Malalasekera, 2007, fig. 13.2)	29
Figure 3.15: Angular discretization and ray representation in the DTM (Versteeg & Malalasekera, 2007, fig. 13.6).....	30
Figure 3.16: Principle of the DTM (Versteeg & Malalasekera, 2007, fig. 13.7).....	31
Figure 4.1: The flare system on the platform	33
Figure 4.2: KFX model of the platform	34
Figure 4.3: Graphical presentation of measuring point locations	35
Figure 4.4: τ as a function of distance.....	38
Figure 4.5: Graphical presentation of release cell setup	40
Figure 4.6: Subdivision of release cells	41

Figure 4.7: Special case.....	42
Figure 4.8: Adjusted locations for LP flare.....	43
Figure 5.1: Picture of flare flames during measurements (SINTEF Energiforskning AS, 2006, fig. 38)	45
Figure 5.2: Separately simulated HP and LP flare flames combined in one picture.....	46
Figure 5.3: Flames when HP and LP flare are simulated simultaneously, at actual locations.	47
Figure 5.4: Flames with adjusted LP flare locations	48
Figure 5.5: Radiation level, actual locations	49
Figure 5.6: Deviation, actual locations.....	49
Figure 5.7: Radiation levels, adjusted locations.....	51
Figure 5.8: Deviation, adjusted locations.....	51
Figure 5.9: Locations for radiation level plots with reduced number of CV cells.....	53
Figure 5.10: Radiation level comparison when reducing the number of CV cells	53
Figure 5.11: Radiation level comparison when reducing the number of cells.....	54
Figure A.1: First run of full simulation	A-1
Figure A.2: Results at t = 90s for first run and restarted simulation	A-2
Figure A.3: Results at different times using restart file 90	A-3
Figure A.4: Results using Courant number 10 and 20	A-4
Figure A.5: Result of the sensitivity test of choosing the number of ordinates	A-5

List of Tables

Table 2.1: Permissible radiation levels (American Petroleum Institute, 2007, Table 9)	5
Table 2.2: Parameters affecting the radiation level	6
Table 2.3: CFD techniques for modeling radiative heat transfer (Baukal, 2000, p. 166)	9
Table 3.1: Parameter values used in release cell sensitivity test	22
Table 3.2: Setup in release cell sensitivity test.....	24
Table 4.1: KFX coordinates of flare tips and measuring point locations.....	35
Table 4.2: Given parameter values from SINTEF (SINTEF Energiforskning AS, 2006)	36
Table 4.3: Fuel gas composition used in KFX	38
Table 4.4: Calculation domain boundaries	40
Table 4.5: Setup of release cells.....	41
Table 5.1: Measured radiation levels (SINTEF Energiforskning AS, 2006).....	48
Table 5.2: Simulation time	52
Table 5.3: Simulation time when reducing the number of cells.....	54

1 Introduction

One of the most important safety barriers to avoid accidents on an oil-producing offshore installation is the flare system. The main purpose of the flare is to achieve safe and effective disposal of gases and liquids, at an affordable cost. These gases and liquids are usually flammable, toxic or corrosive and the flare is using combustion to convert the gases and liquids to less harmful compounds. During this process the flare itself becomes a source of hazard due to the flare flame. The main hazard is thermal radiation emitted from the flame as this can harm both personnel and equipment if the levels get too high. The allowable radiation levels are regulated by NORSOK standards, which contain guidelines for maintaining a high level of safety while keeping the costs down (NORSOK, 2008). Examples of personnel injuries if the levels exceed the allowable radiation levels are skin burns, behavioral disorders, heat stroke or even death. In relation to equipment damage, plastic parts and hoses can melt, electronic equipment may malfunction and steel or aluminum constructions can lose their structural integrity (Baukal, 2013, p. 9). In order to design a safe flare system that is in compliance with regulatory requirements, an appropriate model for predicting thermal radiation levels is a very useful tool.

As a high degree of accuracy is needed due to the safety and cost aspect, the modeling of thermal radiation from a flare is challenging. Computational fluid dynamics (CFD) is a popular approach to conduct the modeling and a CFD simulator that can be used for this purpose is Kameleon FireEx (KFX®). Even though this program has been tested and validated against several field-scale cases, the results will largely depend on the users input, e.g. how the fuel release from the flare, ambient conditions and grid configuration are defined. These choices will directly affect the resulting radiation levels, and finding the most optimal approach is usually desired. An approach being optimal means that a high degree of accuracy is obtained within an acceptable simulation time. One way to validate the simulations and determine the accuracy is to compare the simulated radiation levels to measured levels from a real flaring scenario.

The topic of this thesis is modeling thermal radiation levels from flares. The thesis is built up by first giving the background about flare systems, and how radiation levels have been modeled over the years. Following this is a presentation of KFX including numerics, theory of jet modeling and the radiation model used in the program. Then the simulations performed in the thesis are described, giving a detailed explanation of the considerations and assumptions that had to be made. Lastly, the results will be discussed and compared to measured levels from a real flaring scenario, followed by a conclusion.

2 Background

In this chapter basic terminology and facts regarding flares and modeling of thermal radiation is presented.

2.1 Flare Types

The primary function of a flare system is to use combustion to convert flammable, toxic or corrosive gases and liquids to less harmful compounds. When designing the flare system several factors may influence the decisions and the most important are the desired characteristics of the flare flame and costs (American Petroleum Institute, 2007). With respect to space efficiency, elevated flares are most common, which consists of a flare stack with a flare tip mounted on top. One of the most important components in the flare system is the tip, because the diameter and design of the tip affect the flame characteristics, and hence the radiation. Many variations exist and the simplest tip is referred to as a pipe-flare tip, as pictured in Figure 2.1. The structure of this tip is simply a piece of pipe with a flame retention device and a pilot for flare gas ignition. The fuel gas discharge is occurring through one single opening.

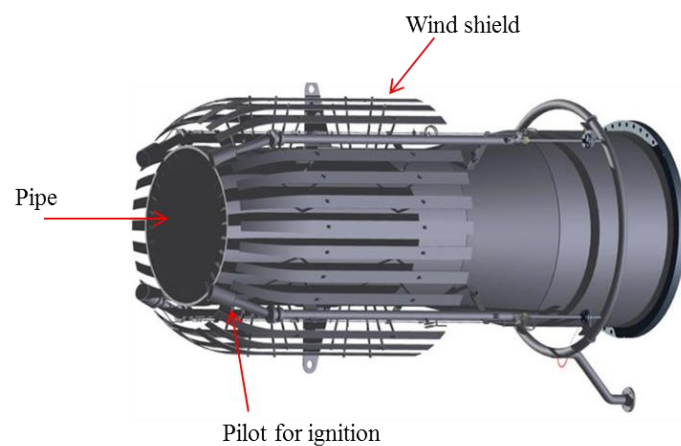


Figure 2.1: Pipe-flare tip (Prema-Service)

More complex flare tips referred to as multiple nozzle flares are also widely used. The tip is then built up by some sort of nozzle arrangement, and the number of nozzles varies from tip to tip. These tips may utilize improved air distribution, steam injection, smoke and noise suppression and other features for cleaner combustion (Schwartz, White, & Bussman, 2013). Two different arrangements are shown in Figure 2.2.

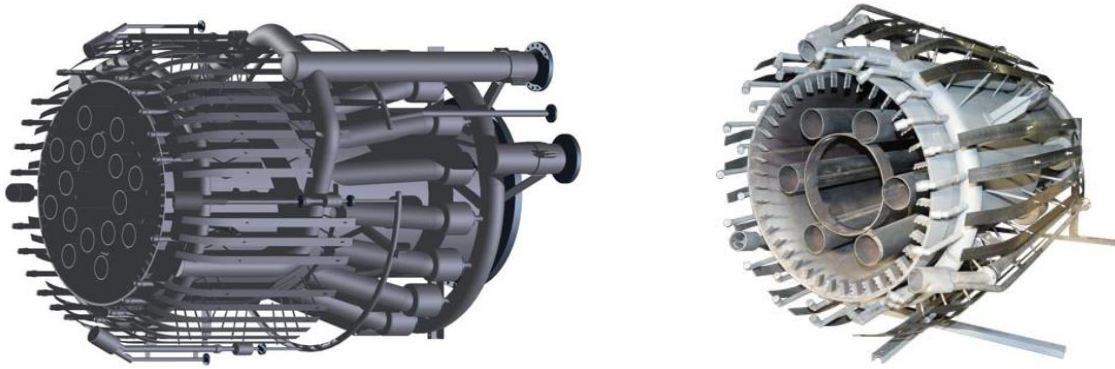


Figure 2.2: Multiple nozzle flare tips (Prema-Service)

In this thesis, an advanced flare system combining two different pipe-flares will be looked at, and more details are given in chapter 4.1.

2.2 Thermal Radiation

Thermal radiation is simply heat transported by electromagnetic waves. It does not require any medium to be transported in, as opposed to heat transported by convection or conduction (Incropera, Dewitt, Bergman, & Lavine, 2013, p. 8). Radiation in general includes a wide specter of wavelengths, but thermal radiation is defined as the portion of the spectrum with wavelengths between $1 \cdot 10^{-7}$ and $1 \cdot 10^{-4}$ m, see Figure 2.3. A flare emits radiation with wave lengths from approximately $0.3 \cdot 10^{-6}$ to $30 \cdot 10^{-6}$ m which is all within the thermal radiation specter and mainly infrared. For comparison, the sun emits radiation with wavelengths from $0.3 \cdot 10^{-6}$ to $3 \cdot 10^{-6}$ m, of which 46 % is infrared (J. White & Bussman, 2012, p. 208).

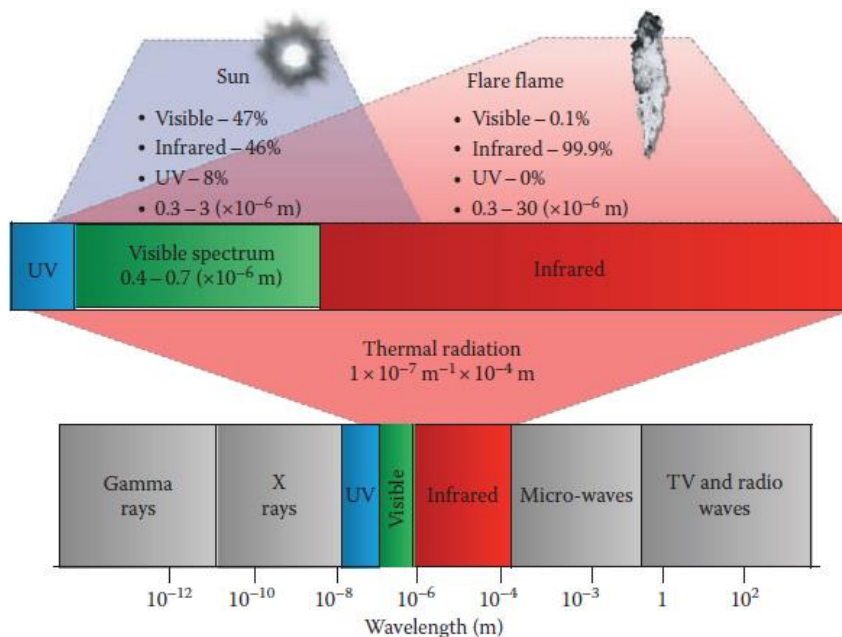


Figure 2.3: Electromagnetic spectrum (J. White & Bussman, 2012, fig. 8.1)

Only solids, liquids and gases at a finite temperature above the absolute zero (0 K) can emit radiation. This means that it is the solids and gases present in the flare flame that emit radiation and the most important are the main combustion products, namely soot, CO₂ and H₂O (J. White & Bussman, 2012, p. 212). The amount of thermal radiation emitted from the flare flame that is received at a specific location is in this thesis referred to as the *radiation level*. This is heat flux and is given in W/m².

To quantify how large radiation levels can be before posing risk to humans, the NORSOK standards are used at the Norwegian Continental Shelf. They are made to ensure adequate safety, cost effectiveness and compliance with the authorities' regulations. For thermal radiation exposure of personnel, NORSOK-S001 refers to the API Standard 521 for recommended threshold limits (NORSOK, 2008), as given in Table 2.1.

Table 2.1: Permissible radiation levels (American Petroleum Institute, 2007, Table 9)

Radiation level (kW/m ²)	Conditions
9.46	Maximum radiant heat intensity at any location where urgent emergency action by personnel is required. When personnel enter or work in an area with the potential for radiant heat intensity greater than 6.31 kW/m ² , then radiation shielding and/or special protective apparel (e.g. a fire approach suit) should be considered. <i>Safety precaution — It is important to recognize that personnel with appropriate clothing^a cannot tolerate thermal radiation at 6.31 kW/m² for more than a few seconds.</i>
6.31	Maximum radiant heat intensity in areas where emergency actions lasting up to 30 s can be required by personnel without shielding but with appropriate clothing ^a
4.73	Maximum radiant heat intensity in areas where emergency actions lasting 2 min to 3 min can be required by personnel without shielding but with appropriate clothing ^a
1.58	Maximum radiant heat intensity at any location where personnel with appropriate clothing ^a can be continuously exposed

^a Appropriate clothing consists of hard hat, long-sleeved shirts with cuffs buttoned, work gloves, long-legged pants and work shoes. Appropriate clothing minimizes direct skin exposure to thermal radiation.

2.3 Parameters Affecting the Radiation Level

There are several parameters that can affect the radiation emitted by a flare, and having knowledge about them is essential to perform accurate calculations of radiation levels. The parameters are as follows (Guigard, Kindzierski, & Harper, 2000):

Table 2.2: Parameters affecting the radiation level

1)	Gas composition
2)	Flame type, geometry and temperature
3)	Emissive and absorptive properties of matter within the flame
4)	Mass flow of flare gas
5)	Flare tip design
6)	Ambient conditions (humidity, temperature and wind)
7)	Soot and smoke formation
8)	Radiation fraction of total heat release

When calculating radiation levels, simplifications must be made. Depending on the chosen model, the listed parameters can be included, excluded, simplified or estimated, giving different results from model to model. It is therefore important to know how the models are treating the parameters, and what weaknesses the models are possessing (Ertesvåg, 2000, p. 34). Often the user does not possess enough information to give correct values to all parameters, thus some has to be estimated. How the parameters are treated in KFX will be presented in chapter 3.4.

2.4 Thermal Radiation Modeling Techniques

The methods used for calculating and modeling thermal radiation from flares have been developed and improved over the years. Different techniques are used for different types of flares, and the complexity of the methods varies widely, ranging from simple empirical methods to more advanced CFD models. In the following the development of some selected approaches is presented.

2.4.1 Empirical Methods

The empirical methods used to calculate thermal radiation from flares can be divided into three main modeling approaches; the single-point model, the multiple-point model and the solid-body model, as illustrated in Figure 2.4 (J. White & Bussman, 2012, p. 217). Common for these models are that they are cheap and easy to perform, as pen and paper usually are sufficient tools.

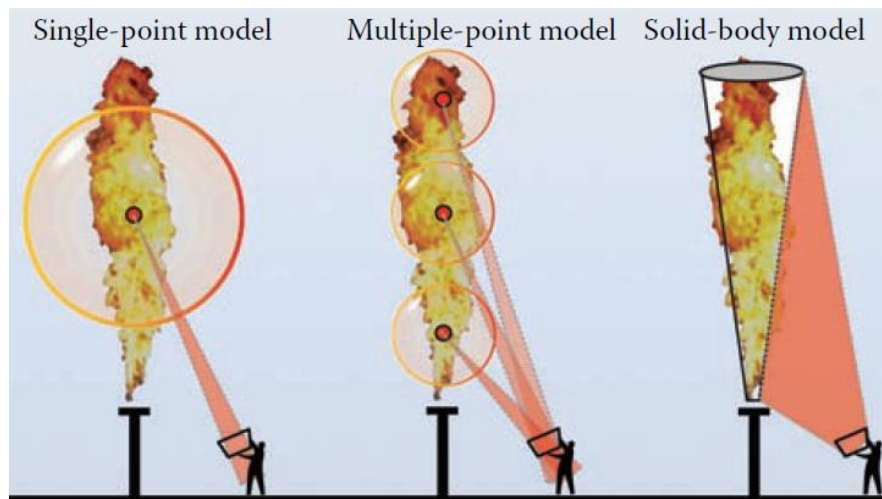


Figure 2.4: Empirical modeling approaches (J. White & Bussman, 2012, fig. 8.12)

One of the simplest of the existing methods, and the most used, is presented in the API standard 521 (American Petroleum Institute, 2007). This method is named Brzustowski's and Sommer's method, and is based on the single-point model. This means that all radiation is assumed originating from one single point within the flare flame, usually the flame centroid, and spread equally in all directions. This method's advantages and disadvantages have been thoroughly discussed in the specialization project that this master thesis is a continuation of (Bjørnæs, 2015). The conclusion of the project was that the method is applicable when a simple subsonic pipe-flare in an environment without complex geometry is to be evaluated, and radiation levels are calculated far away from the flare. The method over predicts radiation levels close to the flare, and this is a well-known weakness. The conclusion is also backed in other literature, like reports from Guigard et al. (2000), Brzustowski and Sommer (1973) and Chamberlain (1987).

Approaches based on the multiple-point model take the flame shape better into account compared to the single-point model. The user can decide how many points to include in the calculations, depending on the desired level of accuracy. Various versions of such models exist, but it is also here concluded that the method possesses weaknesses when calculating radiation levels close to the flare (Crocker & Harper, 1988).

The Shell-Thornton model is probably the most known solid-body model. In this model, the flare flame is represented as a frustum of a cone, as seen to the right in Figure 2.4. Instead of assuming that the radiation is emitted by a single or multiple points within the flame, the radiation is now regarded to be emitted from a solid body with uniform surface emissive power. This approximation allows for more realistic flame behavior, and provides more accurate results close to the flare where the single- and multiple-point models have weaknesses (Chamberlain, 1987). A software tool named Frustum owned by Statoil, where the Shell-Thornton model is implemented, has been developed by Computational Industry Technologies AS (ComputIT). The program will not be examined in this thesis, but it is mentioned as a good alternative in cases where Brzustowski's and Sommer's method is insufficient and a full KFX simulation is excessive (Evanger & Vembe, 2011).

2.4.2 CFD

Even though the mentioned well-established empirical methods are still widely used, the popularity and interest of CFD has increased over the last years, in line with the development and accessibility of computational power. Simulating radiation using CFD is considerably more expensive and time-consuming than using the empirical methods, as it usually requires trained personnel, licenses and software. In return, CFD allows for more complex geometries and extended applicability where the empirical methods are presumed invalid, which is of importance when complex flare systems are to be looked at. Simulating radiation is not an easy task, as the phenomenon of radiative transport is a 6D problem depending on location (coordinates in a 3D domain; x , y and z), direction (two different angles; θ and ϕ) and wavelength (varying from 0 to ∞) (Versteeg & Malalasekera, 2007, p. 426). The CFD procedures that are available vary widely and they all have weaknesses and strengths.

One of the first general method for handling the radiation transfer equation is known as the Hottel's zone method (Hottel & Sarofim, 1967). In this method, the calculation domain is divided into isothermal volume and surface area zones. An energy balance is then put up to calculate the radiative exchange between any two zones, and a set of simultaneous equations of the unknown temperatures and heat fluxes are obtained (Modest, 2003, p. 539). The method was widely used earlier due to lack of better methods that included information regarding reactions in the flow and that could handle more complex geometries.

Some models that may resemble the zone method are the so called flux models. Many variations exist but the basic principle is that the models are based on a discrete representation of the directional variation of the radiative intensity. The equation of transfer is then solved for a set of discrete directions spanning a total solid angle range of 4π (Modest, 2003, p. 498). This model also has limitations in relation to handling complex geometries.

To overcome the mentioned models limitations on complex geometries, Monte Carlo techniques have been developed. Monte Carlo is a collective name for techniques that use statistical sampling procedures to solve a mathematical problem (Modest, 2003, p. 645). A Monte Carlo method for solving radiation problems usually involves the tracing of a large number of randomly released energy bundles and how they are affected by absorptive, emissive and scattering properties in the domain. The method is independent of coordinate system and is therefore applicable to complex geometries (Versteeg & Malalasekera, 2007, p. 427). An overview of advantages and disadvantages of the mentioned methods are listed in Table 2.3.

Table 2.3: CFD techniques for modeling radiative heat transfer (Baukal, 2000, p. 166)

	<i>Advantages</i>	<i>Disadvantages</i>
<i>Zone method</i>	Accounts for inhomogeneities in temperature and concentration of gases	Cumbersome; restricted to simple geometries, does not account for spectral information and is not compatible with numerical algorithms for solving transport equations.
<i>Flux models</i>	Higher order approximations are accurate, accounts for spectral information and are compatible with numerical algorithms for solving transport equations.	Time consuming, requires an iterative solution of finite-difference equations and simple flux approximations are not accurate.
<i>Monte Carlo</i>	Applicable on complex geometries and absorption/scattering of particles can be accounted for.	Time consuming and not compatible with numerical algorithms for solving transport equations.

As the only procedure for calculating radiation levels available in KFX is the discrete transfer method by Lockwood and Shah (1981), this is the only one that will be discussed in detail. The full presentation is given in chapter 3.4. The procedure takes advantage of the strengths of the three types of modeling approaches listed above, and manages to exclude most of the weaknesses associated with them (Cumber, 1995).

3 KFX

The selected CFD simulator used to calculate radiation levels from a flare system in this thesis is KFX, which is one of the most used computer programs for simulating fires in the oil and gas industry. It is now developed by ComputIT, but was originally developed at NTNU and SINTEF Energy, starting in the seventies. The simulation software has since been continuously upgraded and tested against a wide range of large scale test cases (B.E. Vembe et al., 2001). In this chapter, the theory behind the solution procedures in KFX is presented. First a short overview of the numerics is given, followed by theory regarding the modeling of free jets and finally a detailed description of the radiation model is presented.

3.1 Numerics in KFX

KFX uses the finite volume method (FVM) to solve averaged basic transport equations from fluid dynamics and simulate flare behavior (B.E. Vembe et al., 2001). FVM is a numerical algorithm that consists of the following four steps (Versteeg & Malalasekera, 2007, p. 3):

- 1) Divide the calculation domain into discrete control volume cells
- 2) Integration of the governing equations of fluid flow over all the control volumes in the domain
- 3) Discretization of the resulting integral equations into a system of algebraic equations
- 4) Solving the algebraic equations by an iterative method

A short presentation of the steps will now be given. As the main focus of this thesis is radiation modeling and grid configuration, many details of the numerics will be excluded. The overview is meant to give the reader an introduction to how KFX is built up without going in depth and further details can be found in the user manual (B. E. Vembe et al., 2014).

3.1.1 The Staggered Grid

The first step in the FVM is to divide the calculation domain into discrete control volumes (CV), creating a Cartesian grid. The grid used in KFX is a so called *staggered grid*. Figure 3.1 shows a typical two-dimensional staggered grid as it is presented in Versteeg and Malalasekera (2007, p. 188).

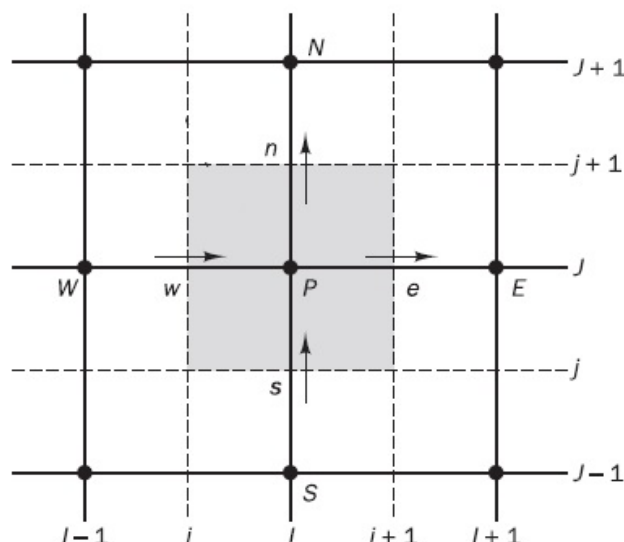


Figure 3.1: Staggered grid in two dimensions (Versteeg & Malalasekera, 2007, fig. 6.5)

The reason for using this type of grid is to avoid storing values of velocity and pressure at the same nodes, as this can cause prediction of non-physical behavior of the pressure field. In the staggered grid, scalar quantities such as pressure, temperature etc. are stored at ordinary nodal points, indicated by P , N , S , W and E in Figure 3.1 and velocities are stored at the cell faces, indicated by n , s , w and e . In a three dimensional grid, the indices T , B , t and b (top and bottom) is also used. It is seen that the dashed lines mark the borders of the velocity control volumes and the solid lines indicates the grid of the scalar control volumes. Figure 3.2 shows a clearer subdivision of the two types of control volumes, using velocities u and v in x - and y -direction as example.

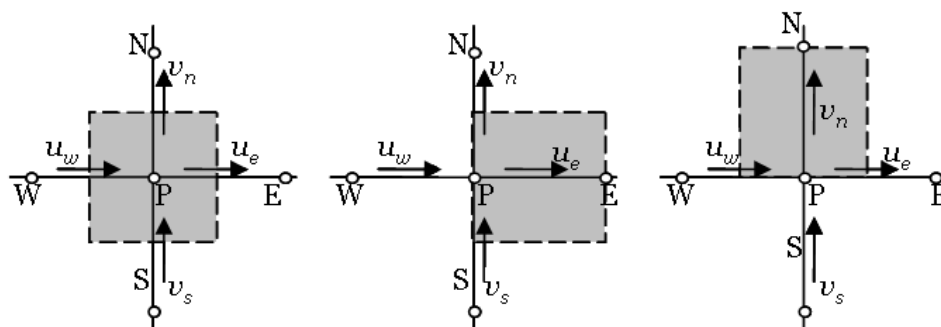


Figure 3.2: Scalar control volume, u -control volume and v -control volume (Thermal-FluidsCentral, 2010)

The user must in KFX decide how many control volumes the calculation domain should be divided into. If a complex geometry or phenomenon is to be resolved, small control volume cells are required, often in combination with a higher amount of cells in the domain. The smaller the cells are, the more accurate solution can be obtained, but this usually causes longer simulation time. Therefore, the tradeoff between accuracy and simulation time is a highly relevant issue when using CFD. On a general CFD project in the industry, over 50 %

of the time is spent on grid configuration, so this is a time consuming and important step (Versteeg & Malalasekera, 2007, p. 3).

3.1.2 Discretization

The transport equation for a general property ϕ , e.g. mass, energy, momentum etc., can be written as (Ertesvåg, 2000, p. 8):

$$\frac{\partial(\rho\phi)}{\partial t} + \frac{\partial}{\partial x_j}(\rho\phi u_j) = \frac{\partial}{\partial x_j} \left(\Gamma_\phi \frac{\partial \phi}{\partial x_j} \right) + S_\phi \quad (3.1)$$

The two terms on the left hand side are the rate of change of property ϕ in time and the convective transport of ϕ , respectively. On the right hand side is the diffusive transport term where Γ_ϕ is the diffusion coefficient of the specific property ϕ , and S_ϕ is the source term. The source term can be sources or sinks of property ϕ caused by other effects than what is included in the three other terms, e.g. external energy generation etc. Any governing equation on the form like equation (3.1) can be discretized by integration over the control volumes in the staggered grid. The equation after discretizing and integrating is given as:

$$\frac{(\rho\phi - \rho^\circ\phi^\circ)}{\Delta t} \Delta V + J_e - J_w + J_n - J_s + J_t - J_b - S_\phi \Delta V = 0 \quad (3.2)$$

Here the superscript $^\circ$ indicates conditions after previous time step, Δt is the current time step and ΔV is the volume of the current control volume cell. J_e , J_w , J_n , J_s , J_t and J_b are the total fluxes through the indicated control volume surfaces. In order to solve this equation it has to be put on the form of a system of linear algebraic equations. To obtain this, KFX uses the so-called second order upwind differencing scheme, which will not be explained in detail here. The resulting predicted value of ϕ at a given point P is given by:

$$a_P \phi_P = \sum a_{nb} \phi_{nb} + b \quad (3.3)$$

where a and b are coefficients. The subscripts P and nb is referring to the center point of the current control volume cell, and the neighboring cells, respectively. The coefficient a is determined by neighboring flux terms, and b is determined by the contribution of the sources from the neighbor's neighbor (B.E. Vembe et al., 2001).

3.1.3 The SIMPLEC Algorithm

To solve the algebraic transport equations on the form like equation (3.3) on the staggered grid, an iterative method has to be chosen. In KFX the SIMPLEC (Semi-Implicit Method for Pressure-Linked Equations Consistent) algorithm is used (B.E. Vembe et al., 2001). The algorithm is a guess-and-correct procedure that calculates the property values on the staggered grid. The flowchart of the procedure shown in Figure 3.3 is a modified combination of Figure 6.6 and 8.10 in Versteeg and Malalasekera (2007).

To initiate the algorithm, a guessed pressure field p^* is applied. This value is guessed based on the users input to the program and is used to solve the discretized momentum equations to find the velocity components u_i^* . The correction p' is defined such that the correct pressure is given by:

$$p = p^* + p' \quad (3.4)$$

and u_i' is defined in the same way. After substituting the correct pressure p in the discretized momentum equations, the correct velocities u_i are obtained. Using these values all other discretized transport equations can be solved. Then it is checked whether $t \geq t_{max}$ and if not the algorithm uses the calculated values as new guessed values and start over again at the next time step. t_{max} is a limit defined by the user.

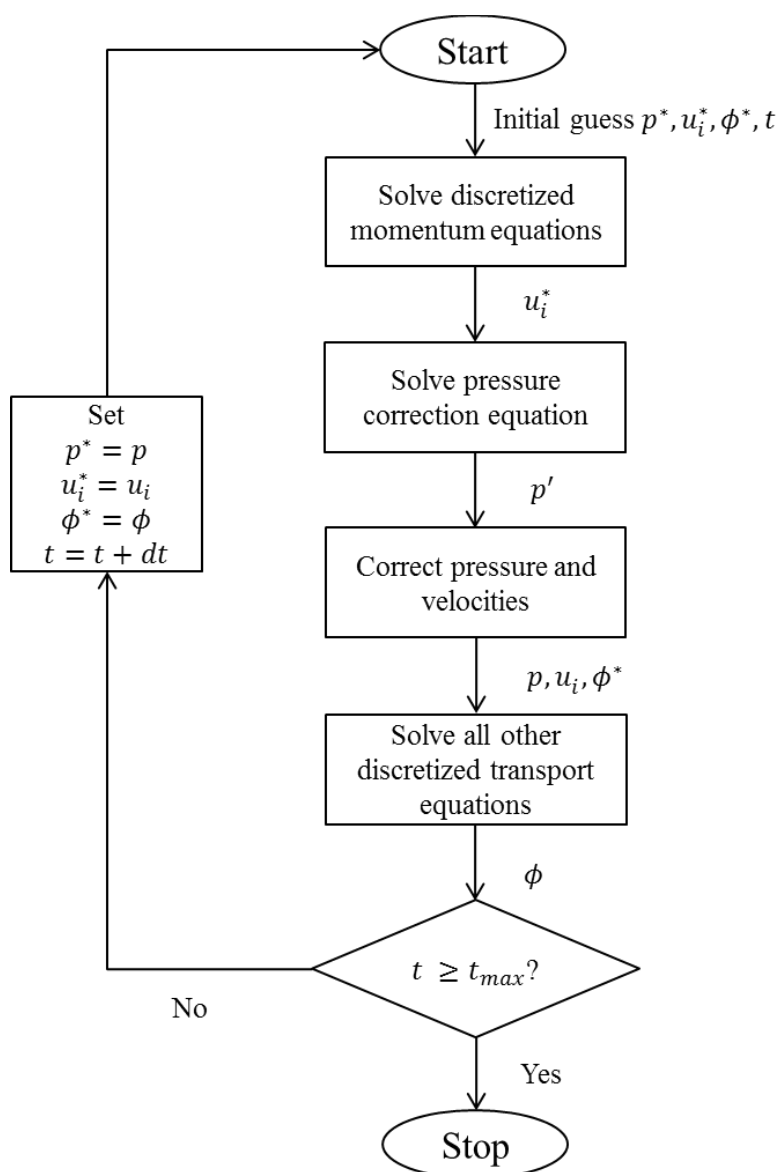


Figure 3.3: Flowchart of the SIMPLEC algorithm (Versteeg & Malalasekera, 2007, fig. 6.6 and 8.10)

There is a built in time step generator in KFX which produces time steps that will ensure stability and accurate time development. The Courant number criterion is used to determine the time step dt , and the criterion is as follows:

$$C = U \frac{dt}{dx} \quad (3.5)$$

Here C is the maximum Courant number, U is the maximum velocity in the domain, i.e. the release velocity at the flare tip exit and dx is the smallest control volume cell length in the domain. This criterion will ensure that no fluid particle travels longer than the control volume cell length multiplied with the Courant number during one time step. It is recommended by ComputIT to use a maximum Courant number of 10 - 20 for flaring scenarios (B. E. Vembe et al., 2014). If the calculated time step is outside specified minimum or maximum limits, these will be used instead.

As seen from the criterion there is two ways of increasing the time step, leading to reduced total simulation time. As the release velocity is fixed for a given release, one can either increase the length of the smallest cell in the domain or increase the Courant number. Both actions has been examined in this study and the effect of increasing cell length is discussed in chapter 3.3.1 and a sensitivity test regarding the Courant number is described in the appendix.

3.2 Equivalent Jet Exit

When modeling radiation from a flare, the flare flame should be simulated as real as possible, starting with the fuel discharge from the flare tip. In order to define correct initial conditions for the fuel discharge in KFX, some theory regarding jet behavior is required. When gas from a high pressure reservoir is discharged to the atmosphere at a much lower pressure, two different situations can occur depending on the Mach number at the nozzle exit. The Mach number is defined (F. M. White, 2011, p. 308):

$$M = \frac{U}{c} \quad (3.6)$$

where U is the release velocity of the fuel discharge and c is the local speed of sound. If the Mach number is $0 \leq M < 1$ the flow is *subsonic* and is in KFX treated as incompressible. On the other hand if $M = 1$ the flow is choked and becomes *sonic* (Anderson, 2007, p. 627). The latter situation results in an underexpanded jet that expands very quickly through interactions between expansion waves and compression waves. The interactions are creating a typical shock structure, as is seen in Figure 3.4.

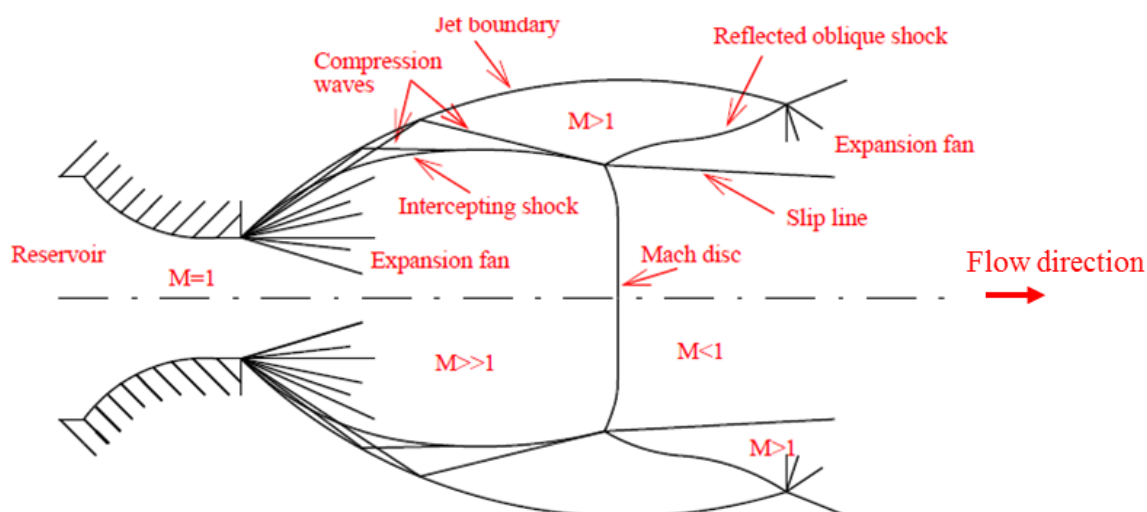


Figure 3.4: Schematic of shock structure (B.E. Vembe et al., 2001, fig. 4.6)

As seen in the figure, an expansion fan forms at the nozzle exit as the flow expands into the low-pressure ambient air. Expansion waves extend to the indicated jet boundary, and reflect as weak compression waves. These compression waves coalesce to form an intercepting shock, which is an oblique shock that separates two supersonic regions, i.e. $M > 1$. The Mach number in the jet core is much higher than the region behind the intercepting shock. A slightly curved shock is formed normal to the flow direction which is referred to as a Mach disk. Behind the Mach disk the flow is subsonic (Crist, Glass, & Sherman, 1966).

When focusing on thermal radiation from the flare, the solver and grid configuration in KFX should be chosen to include the effect of the *overall* dispersion and combustion of the fuel gas. For the subsonic case, no shock structure is created, and the initial conditions of the discharge are equal to the real conditions at the flare tip. For the sonic case on the other hand, manipulation must be carried out. This is because resolving the shock structure requires a very fine grid around the release, in addition to using a compressible solver, and this combination requires a very long simulation time and computational costs increases. To overcome the problem, it is possible to analytically calculate the expanded flow conditions at ambient pressure for the sonic jet behind the Mach disk where the flow has become subsonic, and this new state is called the *equivalent jet exit*. The notation and calculation model is shown in Figure 3.5.

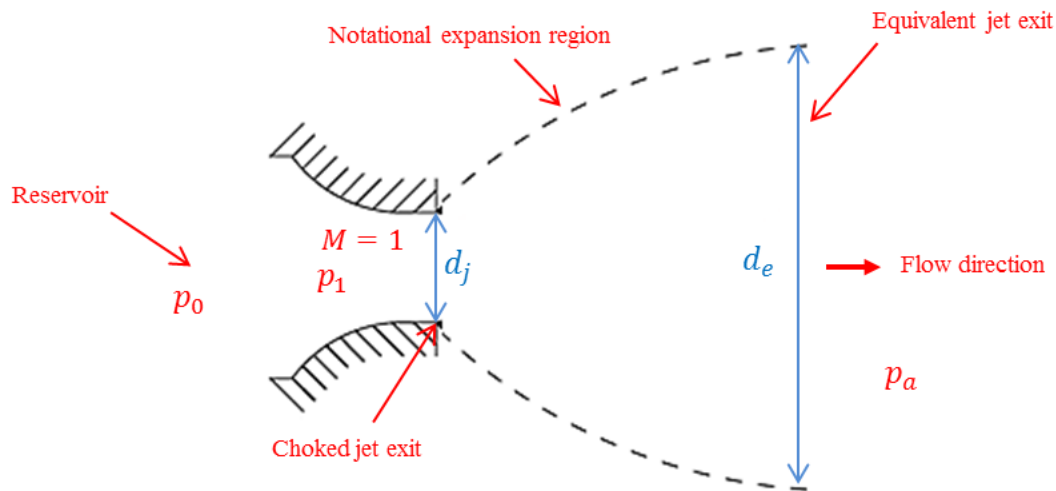


Figure 3.5: Calculation model for the equivalent jet exit (B.E. Vembe et al., 2001, fig. 4.7)

The jet expands through a hypothetical divergent nozzle, referred to as the notational expansion region, indicated on the figure. The viscous forces are negligible at this expansion surface. An equivalent outflow area corresponding to the exit area of the shock structure on a typical nozzle form located where the jet flow has become subsonic is calculated. This is referred to as the equivalent jet exit.

There are several procedures that can be used to calculate the new properties at the equivalent jet exit. The details of the calculations will not be reviewed here, but the approaches are based on the ideal gas law and general theory can be found in e.g. Anderson (2007, pp. 629-638). The specific method used in KFX is the improved version of the pseudo-source concept by Birch, Hughes, and Swaffield (1987). This concept applies the conservation principles of mass, momentum and energy at sub grid level to calculate the equivalent properties of the jet. Note that the equivalent area is larger than the original flare tip exit area. In the sonic case, it is the calculated equivalent properties of the jet that is used as input for further modeling in KFX.

3.3 Release Cells

To set up a flaring scenario, release cells must be defined in KFX. The release cells are the control volume cells in the calculation domain that represent the fuel discharge into the atmosphere, with the characteristics from the equivalent jet exit or the real flare tip, depending on whether the release is sonic or subsonic. It is possible to use one or several cells, and the location of the center point of the cells should be equal to the location of the discharge origin. For the sonic and subsonic case, this means the calculated location of the equivalent jet exit or the real location of the flare tip, respectively. Considering grid configuration, the release cells establish the basis for all other cell sizes as the release cells usually are the smallest in the calculation domain. All other cells are sized with different grow factors based on the release cell sizes.

In KFX two different types of release cells can be used for jet releases; the so-called *supercell* and the *classic release cell*. The difference between them is related to how they treat

entrainment of air. Air entrainment is the process describing how air is mixed with the fuel gas. Using the classic release cell the entrained air is added as an extra mass source in the cell. In the supercell on the other hand, entrained air is taken from the surroundings of the release, and is not added as an extra mass source. The latter gives a more realistic representation of the entrainment process, as flaring usually is non-premixed combustion. The fact that the air is added as a mass source in the classic release cell implies that a larger mass flow is released from the cell and hence a larger release area is required.

To ensure correct mass flow of gas out of the release cells, a correct area of the cell faces must be defined. Figure 3.6 shows a typical control volume cell used to represent the fuel discharge in KFX, regardless of cell type.

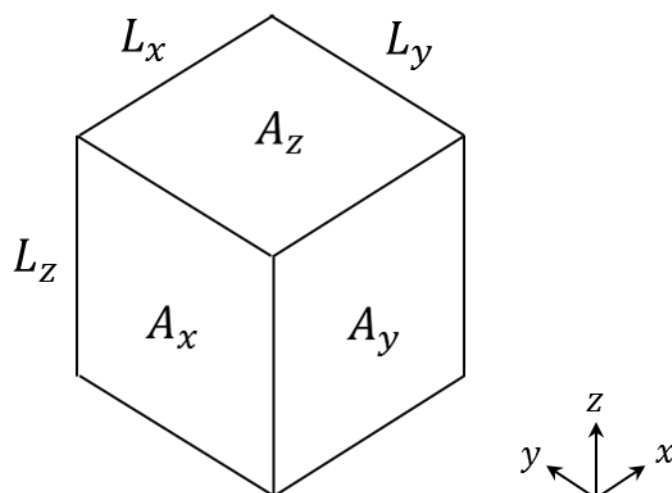


Figure 3.6: Release cell: control volume representing the fuel discharge

The release cell has 6 faces, and the areas of the faces are indicated by A_x , A_y and A_z according to which axis is normal to the plane. The user must correctly define which of the faces the flow should be released through, and how large the areas have to be to match the velocity and density to ensure correct mass flow. From basic fluid mechanics it is known that the mass flow can be expressed as (F. M. White, 2011, p. 143):

$$\dot{m} = \rho AU \quad (3.7)$$

where ρ is the gas density, A is the total release area and U is the total release velocity in the release direction. When the jet release is in the x-, y- or z-direction the fuel is discharged directly through the release cell face that has the x-, y- or z-axis as a normal. Note that the directions are defined in accordance with the grid axis in KFX. The area of this cell face is then equal to the area of the circular outlet with *either* the real flare-tip diameter or the calculated equivalent diameter, depending on whether the release is subsonic or sonic. The principle is demonstrated in Figure 3.7 where the release is in the z-direction, making A_z the release area.

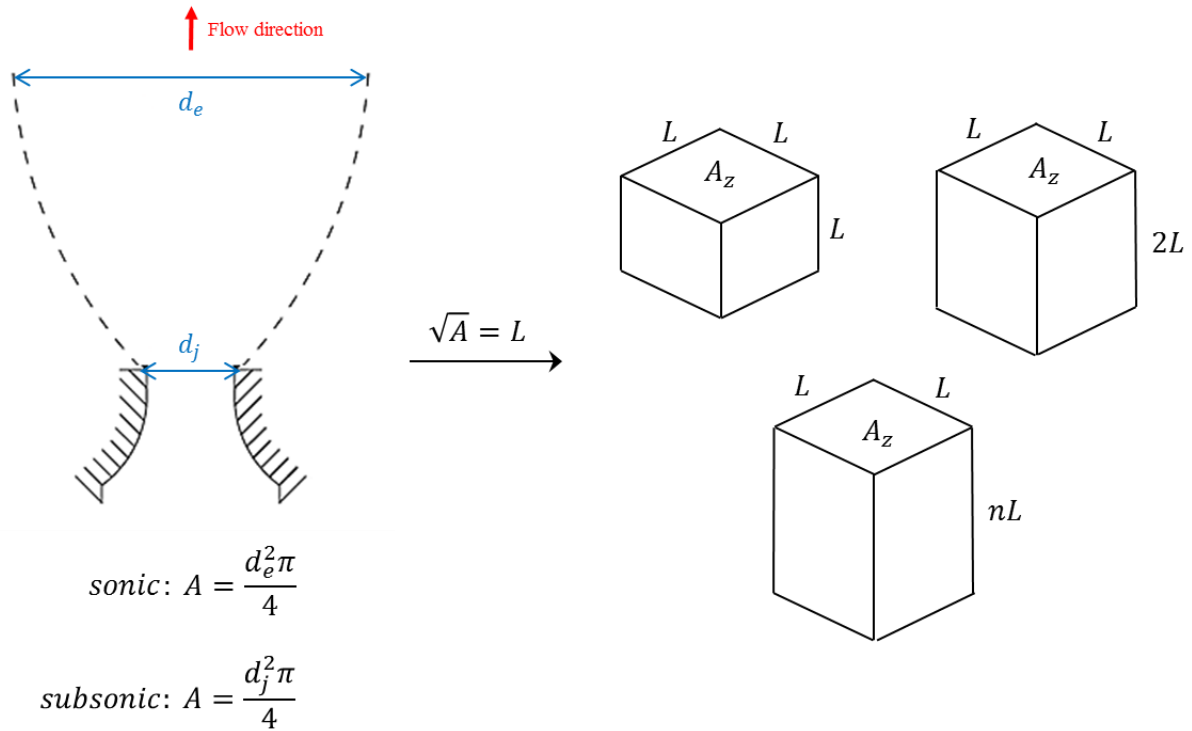


Figure 3.7: Illustration of converting the area of the circular jet exit to a CV cell

In the figure, three different examples of control volumes are made from the circular release area. The fixed parameter in this case when creating the cell is the release area $A_z = L \cdot L$. This means that the length of the control volume can vary in z-direction, regardless of cell type. The reason for wanting to increase this length to make larger control volume cells is that the simulation time will be reduced, in accordance with the Courant number criterion. A sensitivity test regarding the choice of cell size and length in z-direction is conducted in the next chapter.

When the release is inclined, i.e. not in direction of the x-, y- or z-axis, the calculation of release cell face area is not as straight forward as above, and this is where an important difference between the supercell and classic release cell becomes visible. An inclined release has velocity components in at least two directions. The supercell is always releasing fuel through all cell faces that has a velocity component as normal, resulting in *multiple* release surfaces. Using the classic release cell on the other hand, only *one* cell face can be chosen as release surface. To get the correct inclined direction in the latter case, velocity components must be applied normal to the chosen release direction specified in the initial conditions of the cell (B. E. Vembe et al., 2014).

The choice of cell type obviously affects the calculation procedure of release area. Figure 3.8 is illustrating a flare tip inclined at an angle α relative to the ground in the $y = 0$ plane. The release area A is calculated using the flare tip diameter or the equivalent diameter, depending on whether the flare is subsonic or sonic. It is indicated that the total release velocity U can be decomposed into velocities u and w in x- and z-direction.

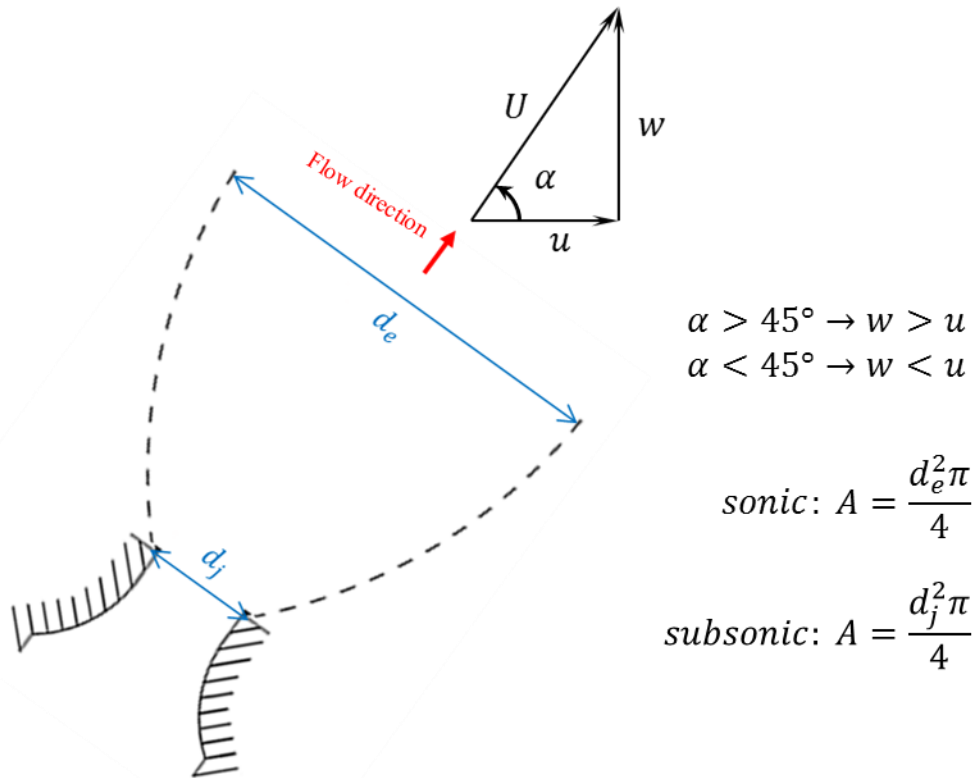


Figure 3.8: Decomposition of release velocity at an inclined flare tip

Using the classic release cell the fuel is as mentioned released through only one of the cell faces. The chosen cell face should be the one with the largest normal velocity, and to obtain correct inclined direction a velocity is applied 90 degrees on the chosen release direction. Using $\alpha > 45^\circ$ as example, w is larger than u and this means that the release should be in z -direction. Applying the principle of continuity it is required that the mass flow out of area A with velocity U must be equal to the mass flow out of area A_z with velocity w having the same density ρ . Using equation (3.7), this is given by:

$$\rho AU = \rho A_z w \quad (3.8)$$

As w is obtained by decomposing velocity U in z -direction, equation (3.8) can be written as:

$$\rho AU = \rho A_z U \sin(\alpha) \quad (3.9)$$

Rearranging gives an expression for the release cell area A_z :

$$A_z = \frac{A}{\sin(\alpha)} \quad (3.10)$$

This release area can now be used to define a correct classic release cell, releasing the fuel in the z -direction with velocity w , and by adding velocity u in the initial conditions of the cell

the correct inclined direction is obtained. Using a classic release cell, the length of the cell in z-direction is not fixed and can be increased.

Using a supercell the fuel is released through two of the release cell faces, instead of one. Using Figure 3.8 as reference, the release should now be in both x- and z-direction regardless of angle α , through the cell faces with area A_x and A_z . The principle of continuity in this case gives:

$$\rho AU = \rho(A_x u + A_z w) \quad (3.11)$$

Expressing u and w by decomposing U and for simplicity defining the release cell to be cubic, i.e. $A_x = A_z$, gives:

$$\rho AU = \rho A_{x,z} (U \cos(\alpha) + U \sin(\alpha)) \quad (3.12)$$

and the areas can be written:

$$A_x = A_z = \frac{A}{\cos(\alpha) + \sin(\alpha)} \quad (3.13)$$

As both A_x and A_z is fixed, it is not possible to increase the cell size by vary any length in any direction, as is possible for the classic release cell. It is clear that the two different cell types result in different release areas for the same inclined release. Figure 3.9 shows an illustration of the fixed release areas marked in red for the two different cell types. Note that the cells are not rotated relative to the grid axis when simulating inclined releases.

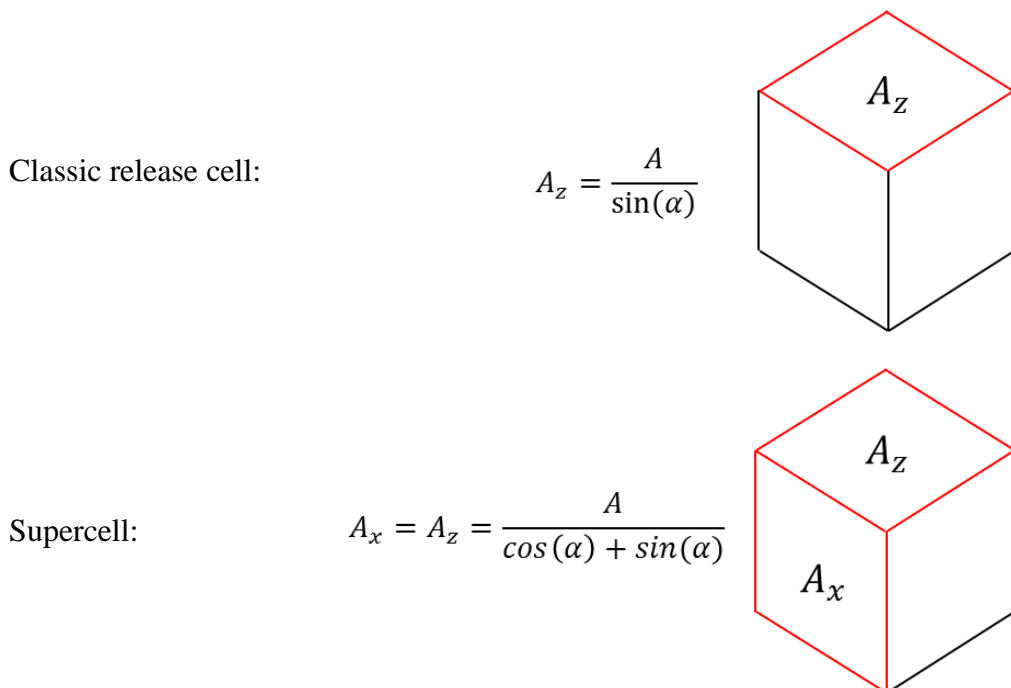


Figure 3.9: Fixed areas at release cells for inclined releases

3.3.1 Release Cell Sensitivity Test

During the specialization project that this master thesis is a continuation of, it was discovered that the number of release cells used to represent the fuel discharge was affecting the resulting radiation level. This has been further investigated, and a sensitivity test has been conducted on a random case. The result of the test sets the basis for how release cells are defined in the other cases simulated in this thesis. The following parameter values were used with methane as the selected fuel:

Table 3.1: Parameter values used in release cell sensitivity test

Ambient conditions:	M_∞	28.97	kg/kmol
	R_H	0	%
	T_∞	10	°C
	U_∞	9	m/s
	Wind direction	90	° (from north)
Flare:	d_j	0.7145 (28.1)	m (")
	LHV	50.02	MJ/kg
	M_j	16.04	kg/kmol
	\dot{m}_j	45	kg/s
	T_j	35	°C

The flare is discharging the fuel in direction of the positive z-axis and is operating at subsonic conditions. Equivalent jet exit characteristics are not applicable, and the release area A_z of the release cell or cells should be equal to the circular area of the flare tip with diameter d_j . The positive y-axis points toward north, which means that the wind is coming from east, i.e. blowing in direction of the positive x-axis. The release has been modeled using 1, 4, 9 and 16 supercells and Figure 3.10 is showing the different subdivisions.

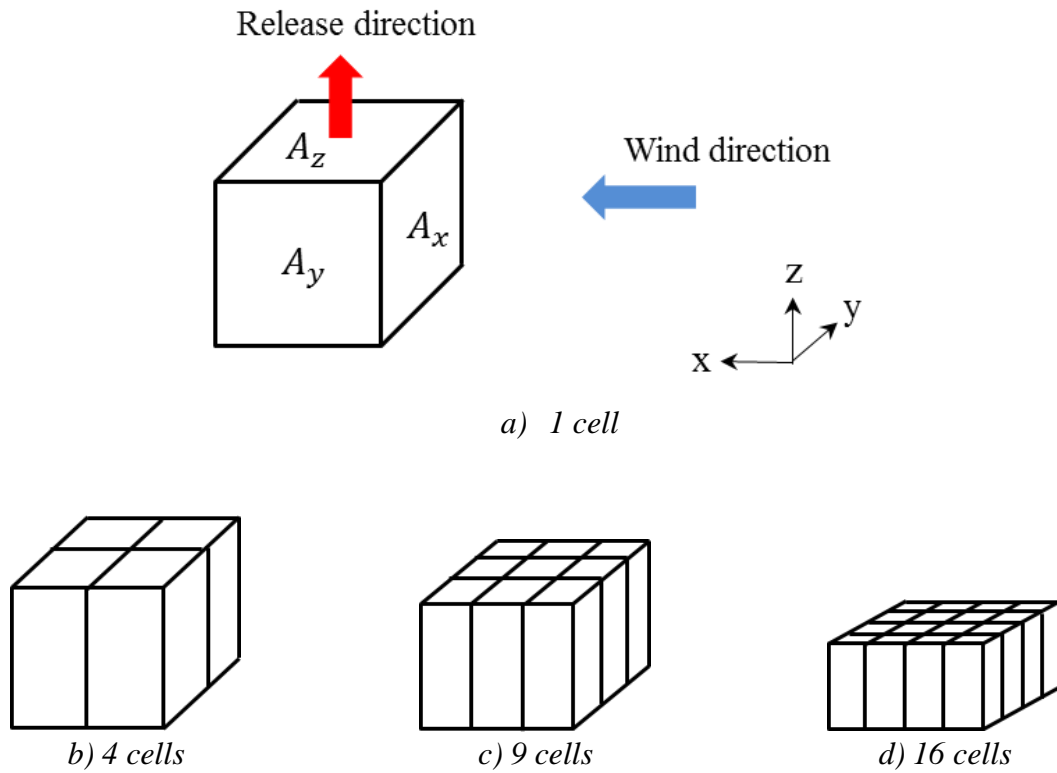


Figure 3.10: Release cell subdivision used in the release cell sensitivity test

As long as the total release area is correct, i.e.:

$$A_z = \frac{d_j^2 \pi}{4} = L_x \cdot L_y = 0.4 \text{ m}^2 \quad (3.14)$$

it is possible to make larger control volume cells by increasing the cell length in z-direction. Increasing the cell size will shorten the simulation time due to the Courant number criterion, as described in chapter 3.1.3. Table 3.2 shows the 7 different setups tested, indicating what number of cells is used and the selected cell sizes, all having total release area of $A_z = 0.4 \text{ m}^2$. The column marked L_z is indicating the length in z-direction compared to the length in x- and y-direction. Note that for all cases $L_x = L_y = L_{x,y}$. If $L_z = L_{x,y}$, the cell is cubic. The simulation time is also included in the table.

Table 3.2: Setup in release cell sensitivity test

Number of cells	Cell size (m)			L_z	Time (hours)
	x	y	z		
1	0.6332	0.6332	1.2664	$2L_{x,y}$	4
	0.6332	0.6332	0.6332	$L_{x,y}$	7
4	0.3166	0.3166	0.6332	$2L_{x,y}$	9
	0.3166	0.3166	0.3166	$L_{x,y}$	16
9	0.2111	0.2111	0.6333	$3L_{x,y}$	9
	0.2111	0.2111	0.2111	$L_{x,y}$	32
16	0.1583	0.1583	0.3166	$2L_{x,y}$	26

The radiation levels have been plotted as a function of x outwards from the flare stack, 100 m below the flare tip. The result is presented in Figure 3.11 where the notation *cubic* and *rectangular* cells refer to whether the release cells are cubic or have increased length in z-direction.

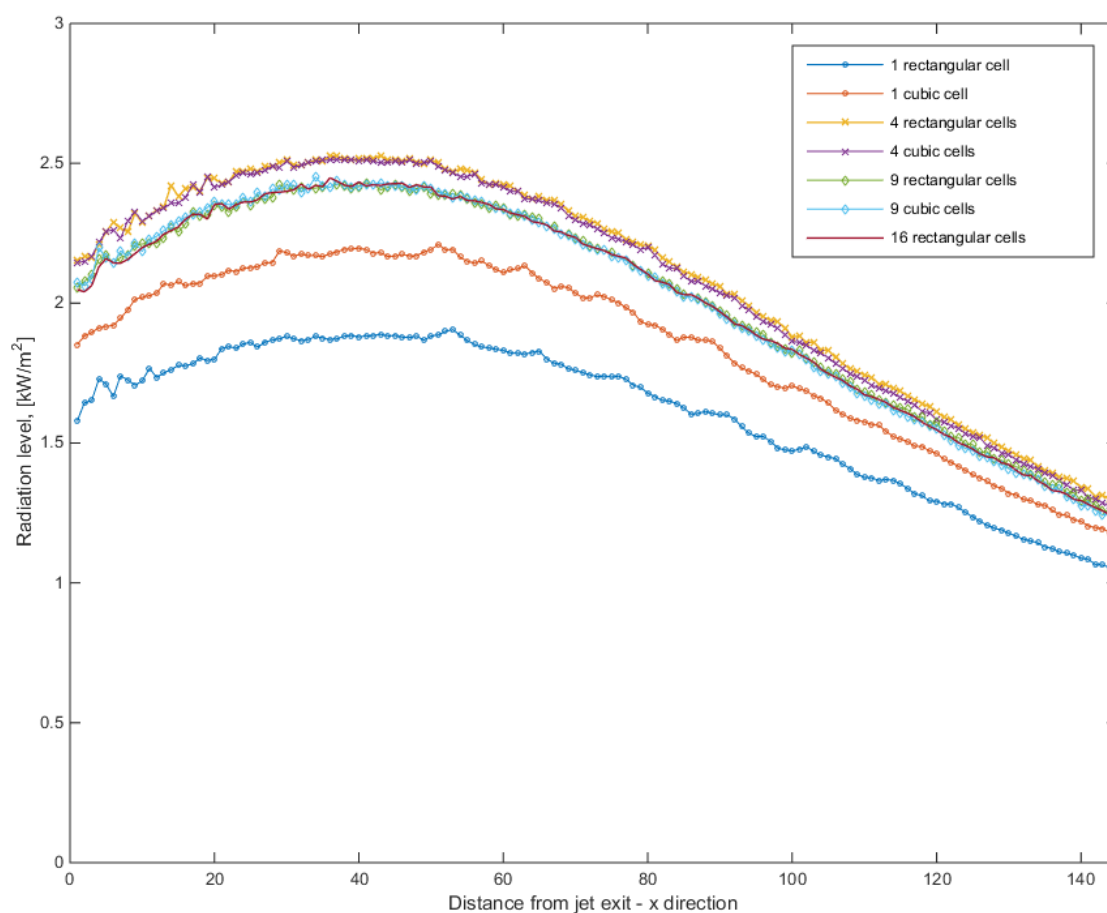


Figure 3.11: Radiation levels from release cell sensitivity test

The choice of release cell subdivision clearly affects the radiation level. It is seen that using 9 and 16 cells gives identical radiation levels. There is a deviation between using 4 cells compared to 9 and 16 but this deviation is small. Using only 1 cell on the other hand, result in

a larger deviation, and is also sensitive to using cubic or rectangular cells. The setups using 4, 9 and 16 cells are not sensitive to increasing the cell size. Far away from the flare, the deviation decreases between all cases. As 9 and 16 cells have the finest grid resolution, it is assumed that these solutions are more accurate than using only 1 cell. Seeing that 9 rectangular cells only use 9 hours to provide the same radiation level as using 9 cubic and 16 rectangular cells there is no need to use smaller cells than this. When using CFD, long simulation time means increased costs, so it is desirable to find the most accurate resolution with the shortest simulation time.

The conclusion of this test is that it is necessary to use more than 1 release cell when modeling radiation levels in a flaring scenario. Using 9 cells, with increased length in z-direction seemed to be the best choice in this particular case, and is considered transferable to similar flaring scenarios.

3.4 The Radiation Model in KFX

To better understand how KFX is calculating radiation levels, some general definitions and facts regarding the modeling of radiation are required. All definitions, equations and figures in chapter 3.4 are reproduced from chapter 13 in Versteeg and Malalasekera (2007) if not stated otherwise.

3.4.1 Equations and Definitions

Radiation is as mentioned energy emission in the form of electromagnetic waves. The *emissive power* E is the rate of heat flow per unit surface area of a radiating surface and is given in W/m^2 . A black-body surface is a perfect emitter, and the black-body emissive power is given as:

$$E_b = \sigma T^4 \quad (3.15)$$

where $\sigma = 5.67 \cdot 10^{-8} \text{ W/m}^2\text{K}^4$ is the Stefan-Boltzmann's constant and T is the absolute temperature of the surface, given in Kelvin. It is seen from the equation that the emissive power is a strong function of temperature, and the higher the temperature, the more radiation is emitted. The *intensity* I is given in $\text{W/m}^2\text{sr}$ and is defined as the rate of heat flow received per unit area perpendicular to the rays and per unit solid angle. The magnitude of I will vary with direction. The black-body intensity is given as:

$$I_b = \frac{E_b}{\pi} = \frac{\sigma T^4}{\pi} \quad (3.16)$$

Not all surfaces can be defined as a black-body and the ratio between the heat flux emitted by a real surface and a black-body surface is called the *surface emissivity* ϵ_s . Hence, the emissive power of a real surface with temperature T_s is given by:

$$E_s = \varepsilon_s \sigma T_s^4 \quad (3.17)$$

and the intensity by:

$$I_s = \frac{\varepsilon_s \sigma T_s^4}{\pi} \quad (3.18)$$

In CFD, the nature of radiation problems is a bit different than other common fluid flows problems. Since the phenomenon of radiation is related to electromagnetic waves, the propagation speed is equal to the speed of light ($3 \cdot 10^8$ m/s). This speed is at least 10^5 times larger than the speed of sound, and this implies that the radiation propagates fast enough to immediately adjust itself to variations in the flow conditions and boundary conditions in the environment. Even though there is no direct coupling between fluid motion and radiation, since radiation does not require a medium to be transported in, the fluid motion will influence the spatial distribution of temperature and species concentrations of other substances in the domain. This will in turn affect the radiation intensity emitted, absorbed and scattered by the substances present in the control volumes, and this is how we have a strong indirect coupling between the flow field of the environment and radiation. If the substances present in the fluid are absorbing or emitting, it will be an extra radiation source term in the energy equation, and there will be changes in the boundary conditions for the energy equation because of the radiation. Figure 3.12 illustrates how a control volume influenced by radiation might look, with boundaries defining area A .

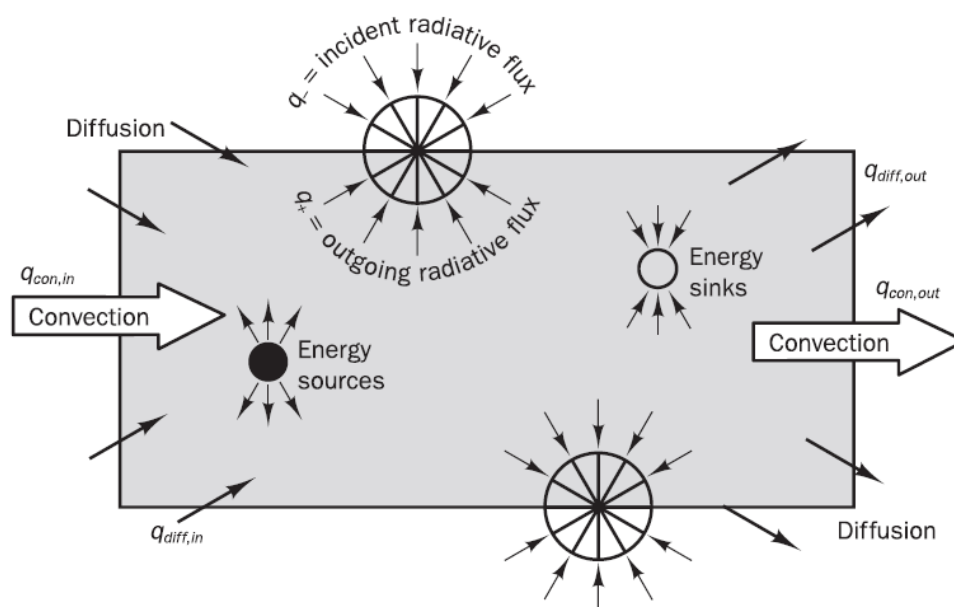


Figure 3.12: Control volume influenced by radiation (Versteeg & Malalasekera, 2007, fig. 13.3)

The energy balance for this control volume is as follows:

$$\int_{CV} S_h dV + \int_{CV} S_{h,rad} dV = \int_A \mathbf{q}_{conv} \cdot \mathbf{n} dA + \int_A \mathbf{q}_{diff} \cdot \mathbf{n} dA + \int_A \mathbf{q}_{rad} \cdot \mathbf{n} dA \quad (3.19)$$

Non-radiative energy source in CV	+	Net radiative energy source in CV	=	Net convective flux through area A	+	Net diffusive flux through area A	+	Net radiative flux across boundaries
---	---	---	---	---	---	---	---	--

and the net radiative source per unit volume $\bar{S}_{h,rad}$ to put into the energy equation is equal to:

$$\bar{S}_{h,rad} = \frac{1}{\Delta V} \int_A \mathbf{q}_{rad} \cdot \mathbf{n} dA = \frac{1}{\Delta V} \int_A (q_- - q_+) dA \quad (3.20)$$

The terms q_- and q_+ are the *incident radiative heat flux* and the *outgoing radiative heat flux*, respectively, given in W/m^2 . These are the radiative fluxes entering and leaving the control volume, and the integral of the difference gives the net radiative heat flux into the control volume, i.e. the net radiative source. To obtain the incident and outgoing heat fluxes, rays coming from or leaving in all possible directions must be included. This is done by integrating the intensity over a unit hemisphere, as shown in Figure 3.13.

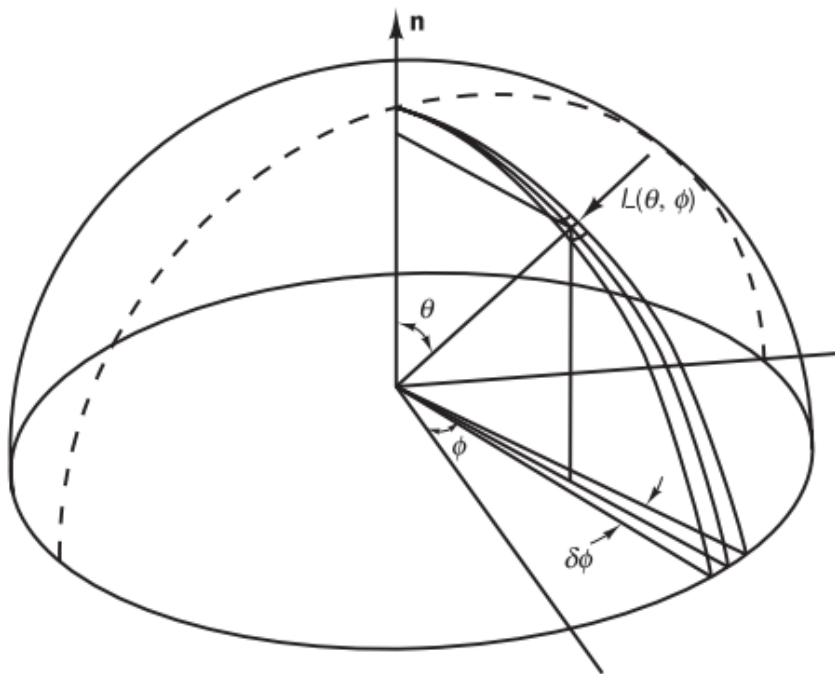


Figure 3.13: Angular notation for equation (3.21) and (3.22). Incoming intensity is used as example (Versteeg & Malalasekera, 2007, fig. 13.4)

The integrals are as follows, where the single integral is performed as integration over a solid angle of 2π steradians, and the double integral is related to Figure 3.13. Note that the two different integrals are just a matter of notation.

$$q_- = \int_{2\pi} I_-(\mathbf{s}) \mathbf{s} \cdot \mathbf{n} d\Omega = \int_0^{2\pi} \int_0^{\pi/2} I_-(\theta, \phi) \cos(\theta) \sin(\theta) d\theta d\phi \quad (3.21)$$

$$q_+ = \int_{2\pi} I_+(\mathbf{s}) \mathbf{s} \cdot \mathbf{n} d\Omega = \int_0^{2\pi} \int_{\pi/2}^{\pi} I_+(\theta, \phi) \cos(\theta) \sin(\theta) d\theta d\phi \quad (3.22)$$

In the single integrals \mathbf{s} is the direction vector of the intensities, which corresponds to the angular direction (θ, ϕ) in the double integrals. As seen in Figure 3.12 the limits for the double integrals are chosen such that the incident radiative flux is calculated over the hemisphere outside the control volume boundary, while the outgoing heat flux is calculated over a hemisphere inside the boundary.

The incident and outgoing intensities, I_- and I_+ , needed in equations (3.21) and (3.22) are found using the governing equation of radiative heat transfer. The equation is as follows, and it governs the changes in intensity at a point along a ray, caused by emission, absorption and scattering in a fluid medium:

$$\frac{dI(\mathbf{r}, \mathbf{s})}{ds} = \kappa I_b(\mathbf{r}) - \kappa I(\mathbf{r}, \mathbf{s}) - \sigma_s I(\mathbf{r}, \mathbf{s}) + \frac{\sigma_s}{4\pi} \int_{4\pi} I_-(\mathbf{s}_i) \Phi(\mathbf{s}_i, \mathbf{s}) d\Omega_i \quad (3.23)$$

Rate of change of intensity per unit path length	=	Emitted intensity	-	Absorbed intensity	-	Out-scattered intensity	+	In-scattered intensity
--	---	----------------------	---	-----------------------	---	----------------------------	---	---------------------------

Here, κ is the absorption-coefficient, σ_s is the scattering coefficient and $\Phi(\mathbf{s}_i, \mathbf{s})$ is the scattering phase function. Note that κ is the coefficient for both emitted and absorbed intensity. This is required due to the principle of local thermodynamic equilibrium (Modest, 2003, p. 282). Figure 3.14 is illustrating a ray in a medium subjected to emission, absorption and scattering processes, where equation (3.23) can be applied.

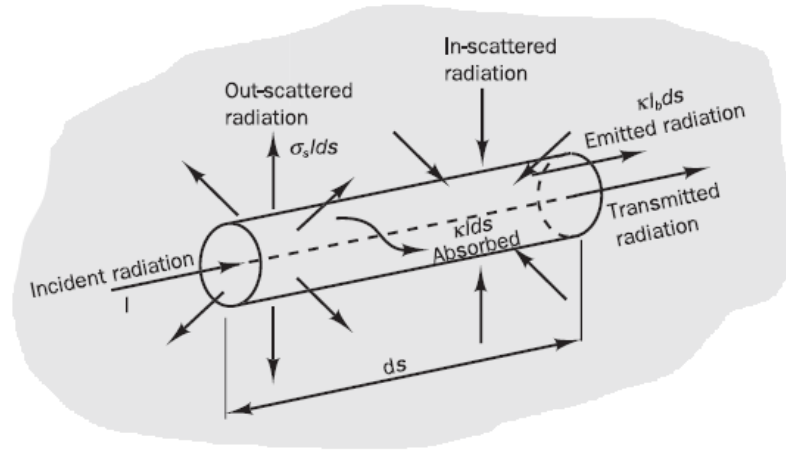


Figure 3.14: Schematic of a ray in a medium with absorptive, emissive and scattering properties (Versteeg & Malalasekera, 2007, fig. 13.2)

When radiation originating from burning gas is modeled, as in this thesis, scattering effects can be ignored, i.e. $\sigma_s = 0$ (Lockwood & Shah, 1981). This implies that equation (3.23) can be reduced to

$$\frac{dI(\mathbf{r}, \mathbf{s})}{ds} = \kappa I_b(\mathbf{r}) - \kappa I(\mathbf{r}, \mathbf{s}) \quad (3.24)$$

where $I(\mathbf{r}, \mathbf{s})$ is the radiation intensity at a given location, determined by position vector \mathbf{r} , in direction \mathbf{s} . This equation is in KFX solved by using the discrete transfer method by Lockwood and Shah.

3.4.2 The Discrete Transfer Method

The solver used in KFX when calculating radiation levels is known as the discrete transfer method (DTM) by Lockwood and Shah (B.E. Vembe et al., 2001). The following procedure is used to solve the governing equation of radiative heat transfer, equation (3.24), and calculate the net radiative heat flux at a specific surface or location.

The first step in this method is discretizing the radiation space into homogenous surface and volume elements. The radiation space is the part of the domain where the radiation rays originate from, which in the simulations in this thesis is the flare flame. Rays are then fired in a direction determined by discretized hemispheres at the surfaces of the surface and volume elements. Figure 3.15 a) shows the angular discretization of the hemispheres in the azimuthal direction, b) shows the polar direction and c) shows the selection of ray directions for a single $d\phi$ angular sector.

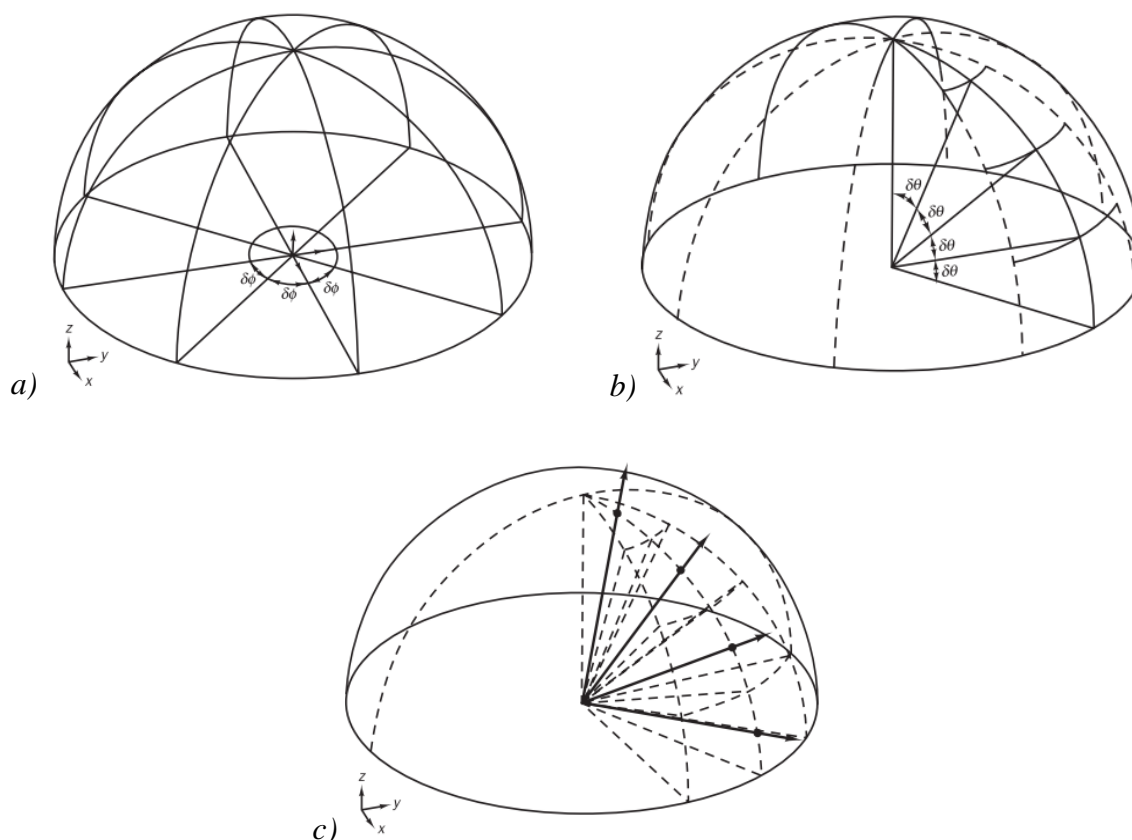


Figure 3.15: Angular discretization and ray representation in the DTM (Versteeg & Malalasekera, 2007, fig. 13.6)

The angles are chosen to be divided into N_θ equal polar angles and N_ϕ equal azimuthal angles giving a total number of solid angles $N_\Omega = N_\theta N_\phi$. The principle of ray tracing is then used through each solid angle element as shown in Figure 3.16.

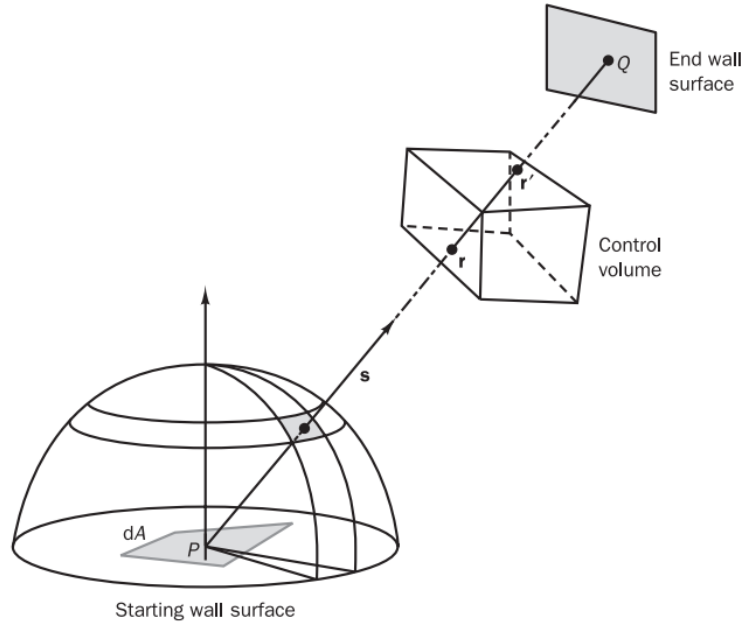


Figure 3.16: Principle of the DTM (Versteeg & Malalasekera, 2007, fig. 13.7)

The ray is traced in the direction of $-\mathbf{s}_k$ until it reaches a boundary, e. g. a solid wall, domain boundary etc., at $\mathbf{r}_L = \mathbf{r} - \mathbf{s}_k L_k$ such that the ray path length from the origin to the boundary is $L_k = |\mathbf{r} - \mathbf{r}_L|$. The subscript k is used to indicate that a specific ray with a specific wave length is traced. To calculate the intensity distribution along the ray, the recurrence relation

$$I_{n+1} = I_n e^{-\kappa \delta s} + I_b (1 - e^{-\kappa \delta s}) \quad (3.25)$$

is used. Here, n and $n + 1$ are used to designate the boundary locations separated by a distance δs for each control volume. Equation (3.25) is the analytical integral of equation (3.24). The initial intensity of the ray is determined at the origin or the starting surface of the ray given by:

$$I_0 = \frac{q_+}{\pi} \quad (3.26)$$

where

$$q_+ = E_s + (1 - \varepsilon_s) q_- \quad (3.27)$$

and the incident radiative heat flux is given by:

$$q_- = \sum_{N_\Omega} I_-(\mathbf{s}) \mathbf{s} \cdot \mathbf{n} \delta \Omega = \sum_{N_R} I_-(\theta, \phi) \cos(\theta) \sin(\theta) \sin(\delta \theta) \delta \phi \quad (3.28)$$

Equation (3.26), (3.27) and (3.28) hence gives the boundary conditions for the surface element where the rays originate from or are arriving at. Here N_R is the number of incident rays arriving at the surface element. The intensity is assumed constant over each finite solid angle. As can be seen from equation (3.27), the value of q_+ depends on q_- . This requires an iterative solution (unless the surface is black; $\varepsilon_s = 1$), and a value for q_- is obtained after the first iteration. The iterations are performed until the solution converges and the negative flux is within a specified limit.

The incident and outgoing radiative heat fluxes can then be calculated at desired surfaces or locations using equation (3.27) and (3.28). The net radiative heat flux is given as the difference between the fluxes.

$$q_{net} = \frac{Q_{rad}}{A} = (q_+ - q_-) \quad (3.29)$$

This is the radiation level that will be calculated at specific locations in a flaring scenario in this thesis. The default parameter values, such as the absorption coefficient etc., used in the radiation model in KFX are tuned towards the most realistic values through several field scale test scenarios. As the user influence of these values are limited, only default values are used in this thesis and the effect of changing the values has not been evaluated.

4 Simulations

The scenario simulated in this thesis is a typical flaring situation on an offshore installation located in the North Sea. Radiation levels have in 2006 been measured by SINTEF at specific locations on the platform deck and under specific ambient conditions (SINTEF Energiforskning AS, 2006). The input parameters used in the simulations are attempted to be similar to the actual conditions during the measurements, and the measured levels are used as validation for the results obtained from KFX.

4.1 The Flare System

The flare system on the platform consists of two pipe-flares, one high pressure (HP) flare and one low pressure (LP) flare, operating at sonic and subsonic conditions respectively. As can be seen in Figure 4.1, the HP flare tip and stack are inclined at 68° relative to the horizontal plane, while the LP flare tip is pointing straight up in the z-direction. The exit diameters of the circular HP and LP flare tips are 0.32 m and 0.30 m, respectively.

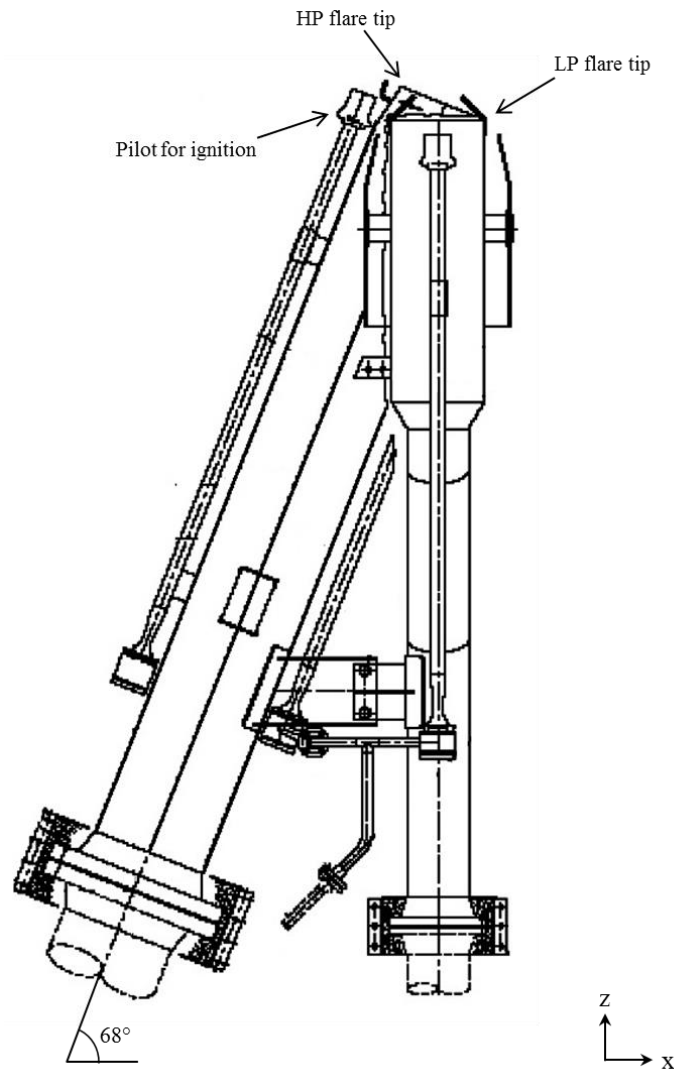


Figure 4.1: The flare system on the platform

4.2 Geometry and Measuring Points

In KFX a very simplified geometry representing the platform is used, consisting of the upper deck, flare stack and platform legs only. The locations where radiation levels are measured are placed with a direct and undisturbed line towards the flare flame, and therefore it is reasonable to remove the process equipment without affecting the result in a significant manner. Figure 4.2 is displaying the geometry.

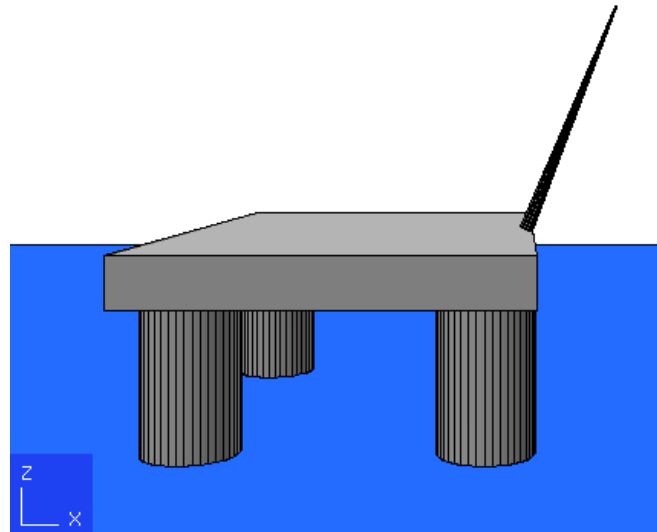


Figure 4.2: KFX model of the platform

The dimensions of the upper deck in x-, y- and z-direction are 80 x 120 x 10 m and the platform legs are stretching down to the sea surface located 42 m underneath the deck. The positive y-axis is pointing towards north. The radiation level measurements were conducted at 6 chosen locations, and the type of gauge used is a so-called Schmidt-Boelter gauge. Figure 4.3 is showing the upper deck seen from above where the 6 locations and the HP flare tip are indicated (SINTEF Energiforskning AS, 2006). Table 4.1 is listing the chosen KFX coordinates.

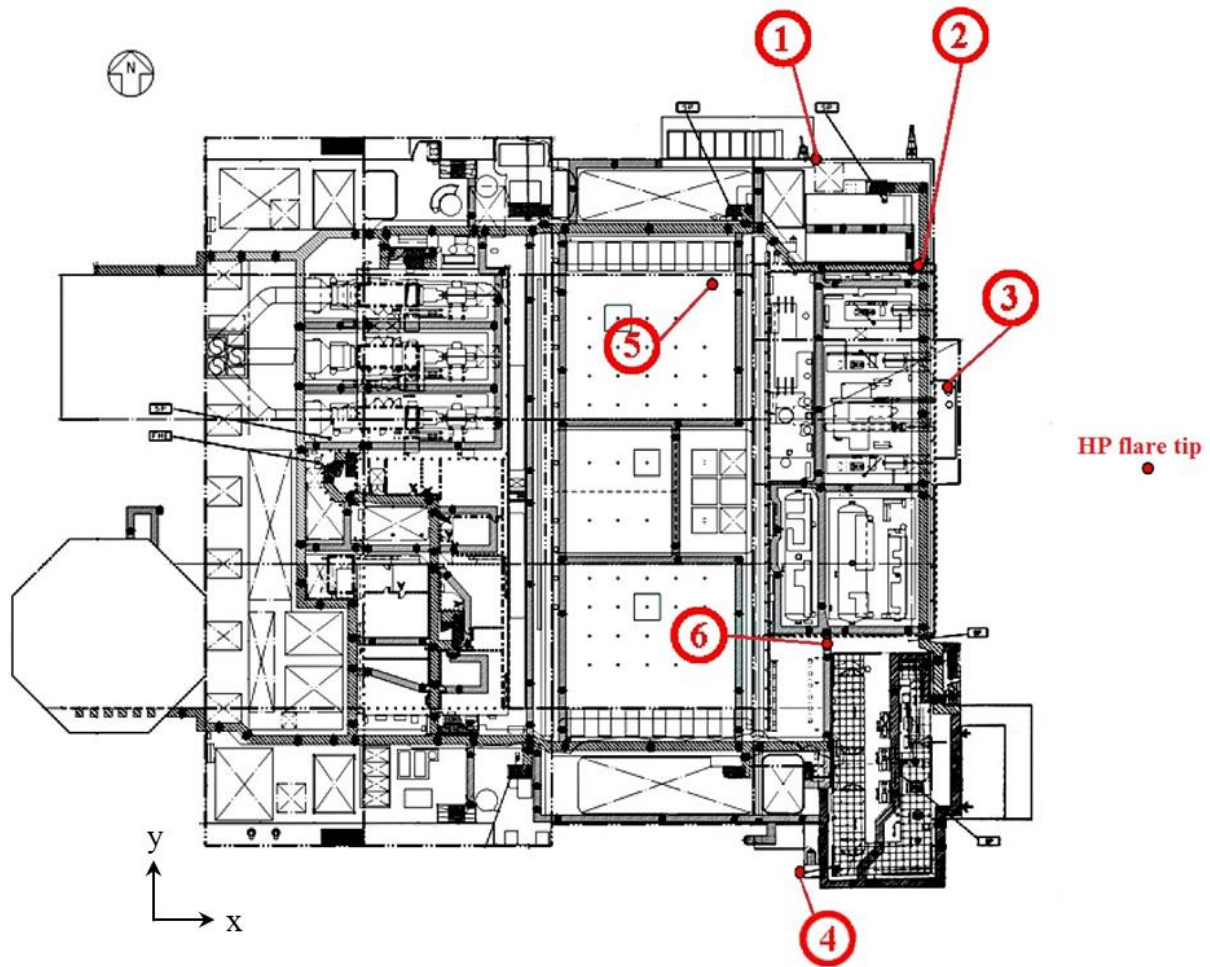


Figure 4.3: Graphical presentation of measuring point locations

Table 4.1: KFX coordinates of flare tips and measuring point locations

Measuring point #	x	y	z
1	-44.3	41.9	4.0
2	-29.3	26.9	11.6
3	-25.3	10.6	3.0
4	-46.3	-57.9	15.6
5	-58.3	23.9	28.0
6	-43.8	-24.9	13.0
HP flare	0	0	53.3
LP flare	0	-0.6	53.2

As is seen in the table, the origin of the chosen KFX coordinate system is set to the same elevation as the upper deck surface, right underneath the HP flare tip. The measuring points are spread around the deck, at different elevations.

4.3 Parameter Values

To limit the degree of uncertainty when trying to replicate the conditions at the specific time the measurements were taken, it is important to use correct input parameter values in KFX. Most of the applicable values were given in the report from SINTEF, and some of these can be directly inserted in KFX. The given parameter values are listed in Table 4.2.

Table 4.2: Given parameter values from SINTEF (SINTEF Energiforskning AS, 2006)

Ambient conditions:	M_∞	28.97	kg/kmol
	R_H	60	%
	T_∞	10	°C
	U_∞	8	m/s
	Wind direction	210	° (from north)
HP flare:	d_j	0.32	m
	LHV	46.4	MJ/kg
	M_j	23.45	kg/kmol
	\dot{m}_j	45.3	kg/s
	T_j	52	°C
LP Flare	d_j	0.3	m
	LHV	46.4	MJ/kg
	M_j	29.0	kg/kmol
	\dot{m}_j	2.8	kg/s
	T_j	52	°C

Some of the parameters have been dedicated a subchapter each for a detailed explanation.

4.3.1 Release Areas

As the HP flare is operating at sonic conditions, the characteristics of the equivalent jet exit described in chapter 3.2 have to be found. This is not relevant for the LP flare, which is subsonic, and the release area is equal to the area of the flare tip exit. The equivalent area of the HP flare is in KFX calculated to be 0.1586 m^2 . This is the area that the release cell design must be based on. Using equation (3.10) and (3.13) inserting the inclination of 68° and the equivalent area, the release cell areas for the two types of release cells can be calculated:

$$\text{Classic release cell:} \quad A_z = \frac{0.1586}{\sin(68)} = 0.171 \text{ m}^2 \quad (4.1)$$

$$\text{Supercell:} \quad A_x = A_z = \frac{0.1586}{\cos(68) + \sin(68)} = 0.122 \text{ m}^2 \quad (4.2)$$

4.3.2 Wind Profile

The wind velocity U_∞ was in the SINTEF report given to be 8 m/s at elevation 112 m above the sea surface, with direction 210° from north, i.e. from the southwest. To simulate realistic wind behavior KFX applies a logarithmic wind profile in the calculation domain. The user has to specify the wind velocity components in x- and y-direction, 10 m above the sea surface, to define a correct profile. The profile of the wind velocity, varying with height z , is developed using Monin-Obukhov similarity theory and is given by (Monin & Obukhov, 1954):

$$U_\infty(z) = \frac{U_*}{\kappa} \left[\ln\left(\frac{z}{Z_0}\right) + 5\frac{z}{L} - 5\frac{Z_0}{L} \right] \quad (4.3)$$

Here, U_* is the friction velocity defined by $U_* = \sqrt{\tau_w/\rho}$, $\kappa = 0.41$ is the von Karman's constant, Z_0 is the surface roughness length and L is the Monin-Obukhov length. The value of Z_0 for a calm sea surface is 0.0002, which is the used value in the simulations (Jacobson, 2005, p. 234). The Monin-Obukhov length is a measure of the stability of the atmosphere, and for neutral conditions L should be infinitely large (Barratt, 2013, p. 36). In the simulations, this value is therefore set to 10 000.

To calculate the x- and y-components of the wind velocity at 10 m above sea surface, the total velocity at 10 m has to be determined. The velocity of 8 m/s measured at 112 m above sea surface is used to find U_* , as this value is constant for all heights. Rearranging equation (4.3) and performing some intermediate calculations the equation gives $U_\infty(10) = 6.52$ m/s. Decomposing this value gives $u_\infty(10) = 3.26$ m/s and $v_\infty(10) = 5.64$ m/s in the x- and y-direction, respectively. These are the input velocities used in the simulations in KFX.

4.3.3 Relative Humidity

The relative humidity R_H of ambient air during the measurements is given to be 60 %. Humid air reduces the radiation levels because of absorption by the water vapors. The inclusion of relative humidity when extracting radiation levels in KFX is applied through a scaling factor called *the transmissivity factor* τ . The factor is defined as:

$$\tau = 0.79 \left(\frac{3000}{R_H \cdot D} \right)^{\frac{1}{16}} \quad (4.4)$$

where D is the distance from the measuring point to the flare flame centroid (Brzustowski & Sommer, 1973). The flame centroid is in KFX determined based on the center of gravity of all sources in the energy equation in the radiation space, i.e. inside the flare flame. The factor is quantifying how large fraction of the total radiation from the flare flame is transmitted through the humid air without being absorbed. For $R_H = 60$ the variation of τ has been plotted as a function of D , seen in Figure 4.4.

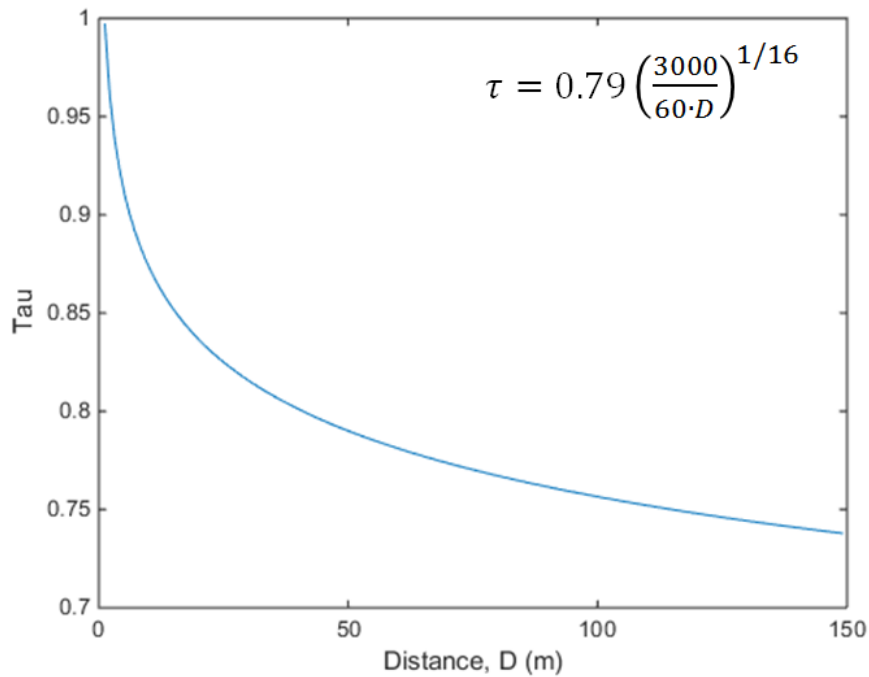


Figure 4.4: τ as a function of distance

It is seen that further away from the flame centroid than 50 meters, which all of the measuring points are, the radiation levels must be scaled by a factor of 0.8 or lower.

4.3.4 Molecular Weight and Lower Heating Value

In KFX the lower heating value (LHV) of the fuel is calculated based on the composition of the fuel gas. The composition of the fuel gas during the measurements is unfortunately not known. To obtain the specified molecular weight combined with the specified LHV as given in Table 4.2 for the fuel gas of the two flares, an educated guess on gas composition had to be made. Natural gas from the North Sea usually consists of mainly methane, with smaller amounts of heavier hydrocarbons, nitrogen and carbon dioxide, so this was the starting point. After performing manual iteration, as close values as possible were obtained. The result is shown in Table 4.3.

Table 4.3: Fuel gas composition used in KFX

	HP flare (vol. %)	LP flare (vol. %)
CH_4	70.0	60.0
C_2H_6	15.0	5.0
C_3H_8	3.6	16.0
C_4H_{10}	9.1	17.9
CO_2	1.6	0.1
N_2	0.7	1.0
M_j (kg/kmol)	23.46	28.99
LHV (MJ/kg)	46.42	46.77

The fact that the gas composition is estimated is obviously a source of error, as the concentrations of species can affect the radiation level from the flame. The species with the greatest influence are soot, H₂O and CO₂ and depending on the gas composition, these combustion products are formed in various amounts.

4.4 Case Setup

4.4.1 *Introductory Remarks*

Simulating a flare system consisting of two flares demands a finer grid around the releases compared to simulating only one flare. When the released flow in addition is inclined, as is the case for the fuel flow from the HP flare, awareness of a common numerical error is important. The second order upwind differencing scheme as is used in KFX might cause the distribution of the transported properties to become smeared in the regions involving inclined flows, leading to physically incorrect results. This phenomenon has a diffusion-like appearance, and is called *false diffusion* (Versteeg & Malalasekera, 2007, p. 150). This type of error can be reduced in three ways; using a finer grid, change the differencing scheme or rotate the grid to be aligned with the inclined flow. As the two latter are not recommended to do in KFX, refining the grid is the only applicable action that can be carried out.

The reason for being aware of this type of error when selecting the grid configuration of the cases simulated in this thesis is because the real locations of the HP and LP flares are very close to each other. This gives reason to believe that it might be hard to find a fine enough grid to fully resolve the HP and LP flare flames without merging them into one flame, while at the same time maintain an acceptable simulation time. As will be discussed later, it is known in advance that the flames were distinctly separated into two flames when the measurements were conducted. Having this knowledge, simulations have been conducted in a logical order, focusing on grid configuration. At first, the two flares have been simulated separately. Then, the two flares have been simulated simultaneously with actual locations starting with a coarse grid which then has been refined around the releases by dividing the release cells into multiple cells. In addition, two cases where the two flares are moved further apart from each other have been tried. The different cases and their setup will in the following be presented.

4.4.2 *Domain Boundaries*

For all cases simulated in this thesis the domain boundaries listed in Table 4.4 are used. The boundaries are chosen in such way that the flow in the domain has enough space both downstream and upstream the platform to fully develop and resolve any wakes downstream the platform. The preliminary number of control volumes in the domain is 1.6 million for all cases, and the effect of reducing the number of cells is investigated in chapter 5.3.1.

Table 4.4: Calculation domain boundaries

	x (m)	y (m)	z (m)
Lower boundary	-250	-150	-42
Upper boundary	300	150	200

4.4.3 Actual Flare Locations

The first cases run in this thesis are aiming at keeping the locations of the two fuel discharges at actual locations according to the coordinates listed in Table 4.1, being (0, 0, 53.3) and (0, -0.6, 53.2) for the HP and LP flare, respectively. A 3D model showing the position of the releases, represented by the yellow cells, together with the clearly inclined stack is seen in Figure 4.5, both from the side and from above. The stack is built up by green, blue, brown and pink cells, which have different properties according to how the flow is passing through them. The stack is in reality a cylinder, and to create this by using rectangular cells the cells are letting the flow through in various amounts and in different directions.

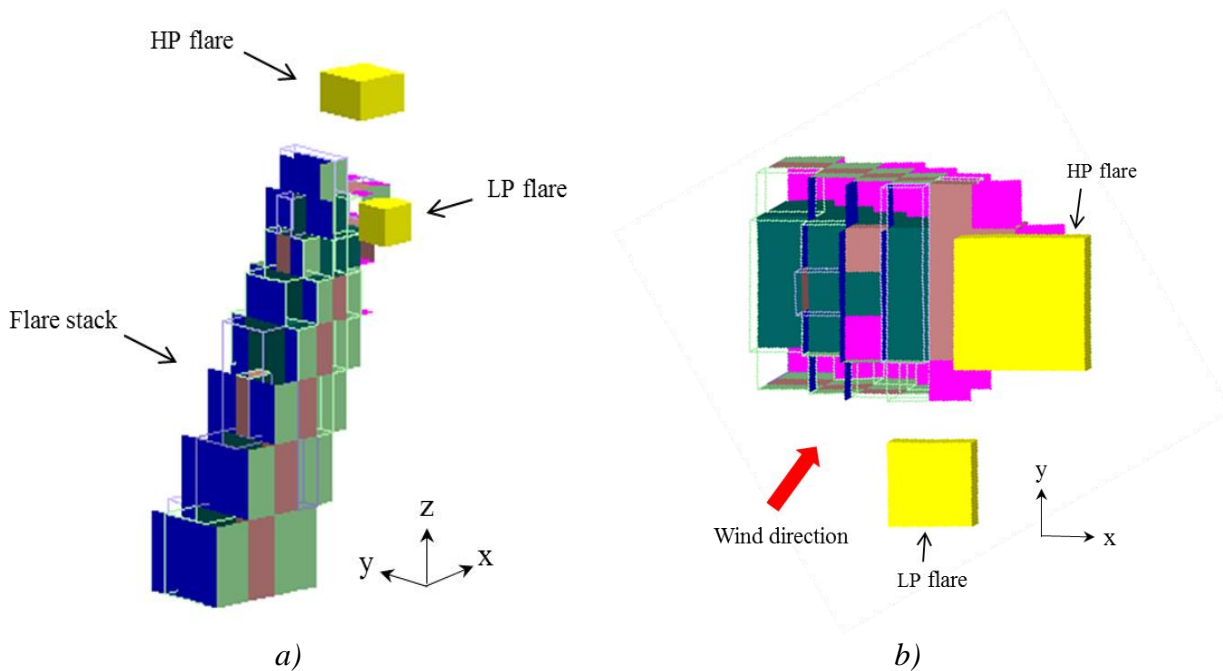


Figure 4.5: Graphical presentation of release cell setup

It is seen from the wind indicator that the LP flare flame will be blown straight into the HP flare flame. This might influence whether it is possible to obtain a fine enough grid resolution to avoid false diffusion while at the same time keep realistic locations and acceptable simulation time. The cases listed in Table 4.5 are the release cell configurations used in the attempt of keeping actual locations, and refining the grid by subdivide the release cells into smaller control volume cells.

4.4 Case Setup

Table 4.5: Setup of release cells

Case #	# of HP flare cells	# of LP flare cells	Cell type
1	1	-	Supercell
2	-	1	Supercell
3	1	1	Supercell
4	1	1	Classic release cell
5	9	4	Classic release cell
6	16	9	Classic release cell

Figure 4.6 shows what the yellow release cells in Figure 4.5 looks like when being subdivided into smaller cells. Note that the classic release cell and supercell does not have the same release area due to different air entrainment, in addition to the fact that the supercell is using both A_x and A_z instead of just A_z when the discharge is inclined, as for the HP flare.

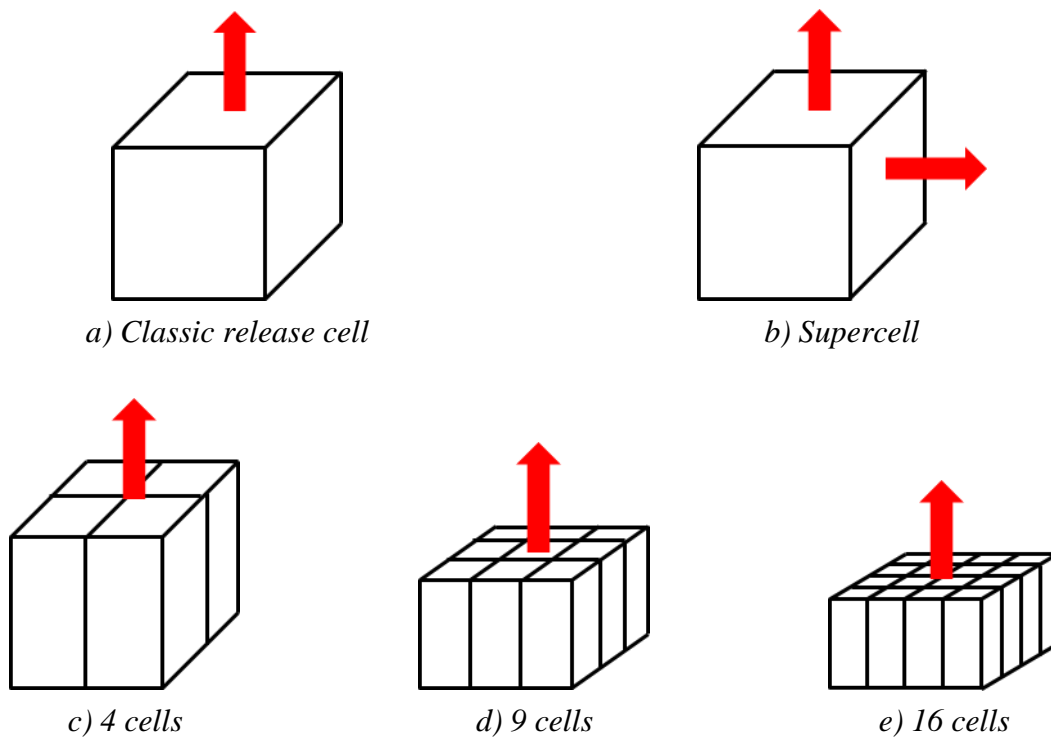


Figure 4.6: Subdivision of release cells

In line with the release cell sensitivity test described in chapter 3.3.1, cubic cells have been used when only 1 cell is representing the release, and rectangular cells with increased length in z-direction are used when subdividing the release into more than 1 cell.

Case 1 and 2 simulates the HP and LP flare separately. This is done to see how the flare flames are behaving when not affecting each other. Simulating only one flare at the time allows for coarser grid, and that is why only 1 release cell is used for each flare.

In case 3 to 6 the two releases are simulated simultaneously. Case 3 and 4 was set up using only 1 cell for the HP flare and 1 for the LP flare, so this grid is also coarse. Case 3 is using supercells and case 4 is using classic release cells, and this is done to reveal differences between the cell types. It is not expected that these grids will be fine enough to resolve the velocity gradients of the flare flames sufficiently. To make a finer grid, case 5 and 6 are using

9 and 16 classic release cells for the HP flare together with 4 and 9 classic release cells for the LP flare, respectively. The reason for using classic release cells when using more than 1 cell is that if supercells are used, the mass flow in x-direction will be flowing into another supercell. This is not recommended, as it may result in un-physical behavior. This is only a problem for inclined releases, which is applicable for the HP flare.

A special case has also been set up, with the configuration as seen in Figure 4.7. The locations of the flares are still actual locations.

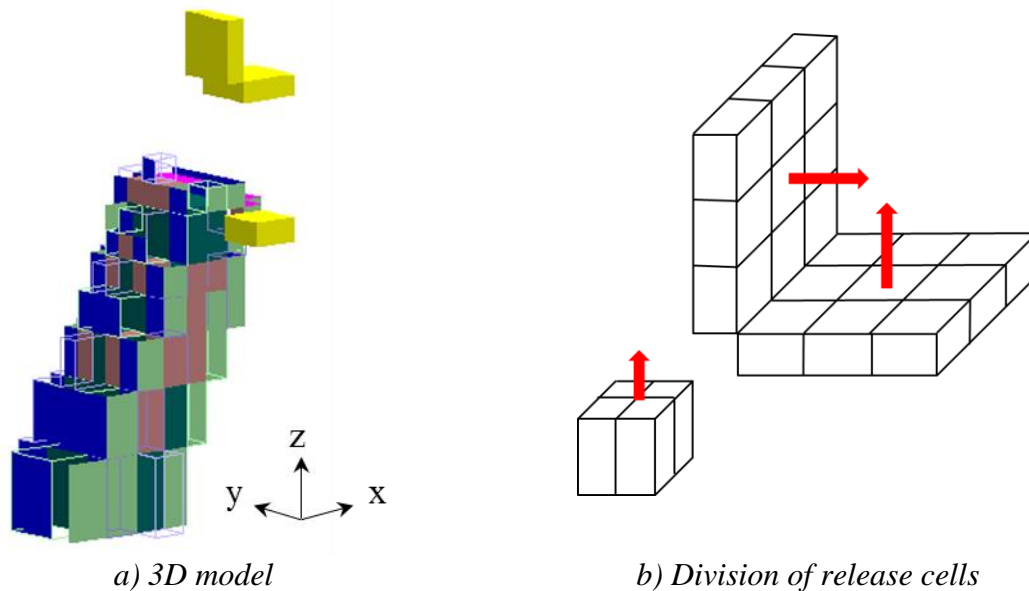


Figure 4.7: Special case

In this case, both the velocities and release areas of the HP flare have been decomposed to one horizontal and one vertical component. This is modeled using one plane normal to the x-direction and one plane normal to the z-direction, both built up by 9 classic release cells each. The areas and velocities are matched such that the total mass flow is correct, and the release obtains the right inclined direction. The LP flare is modeled using 4 cells. This case is set up to find out if it is possible to make other configurations than subdivision of the classic release cell, and what effect this has.

4.4.4 Adjusted LP Flare Locations

Two cases have been run with adjusted locations of the LP flare. The HP flare is still located at the actual coordinates and consists of 9 classic release cells, while the LP flare consist of 4 classic release cells. The LP flare is moved trying to avoid the flame from blowing directly into the HP flare flame, and increasing the distance between the flares will also reduce the possibility of false diffusion. The two new LP flare locations with new coordinates are shown in Figure 4.8.

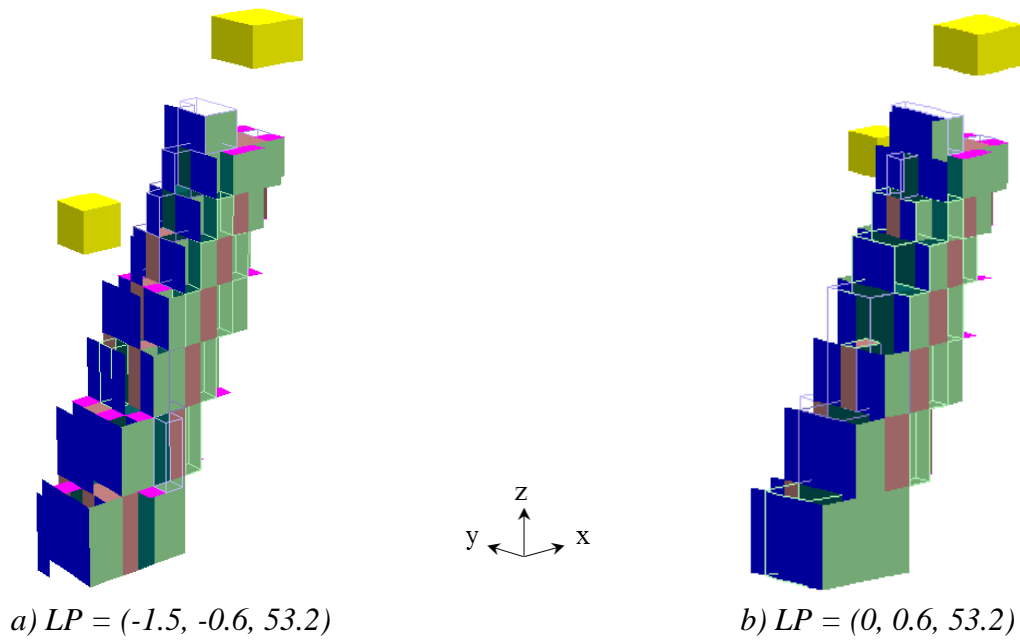


Figure 4.8: Adjusted locations for LP flare

In the case seen in Figure 4.8 a) the LP flare is moved 1.5 m in the negative x-direction. The case seen in b) is mirrored compared to actual locations as the LP flare is moved to $y = 0.6$ instead of the original $y = -0.6$. The latter is done to see the effect of moving the LP flare downstream of the HP flare relative to the wind, without increasing the distance. All other characteristics of the release are naturally kept equal to the cases with actual locations. The effect of moving the LP flare will be discussed when presenting results in the next chapter.

5 Results

5.1 Flare Flames

When using CFD to simulate a scenario, one key issue is to find out if the results are realistic or not. There are many ways of doing this and a starting point can be to look at visible phenomena. During the radiation level measurements used in this thesis, a picture of the flare flames was taken from measuring location number 5. The picture is seen in Figure 5.1.



Figure 5.1: Picture of flare flames during measurements (SINTEF Energiforskning AS, 2006, fig. 38)

Even though the picture does not give an accurate impression of depth, it is clearly seen that the LP flare flame lays lower than the HP flare flame and the two flames are distinctly separated. This is probably happening because the LP flame has lower momentum than the HP flame, and is therefore more affected by the wind causing it to bend in the wind direction. As the HP flare stack is inclined, the flame will bend more in the inclined direction, and it is also less affected by the wind because of higher momentum. To get an impression of whether KFX produces realistic flames, the flame shapes and locations should be similar to the flames in the picture. It is given in the SINTEF report that the flame length of the HP flame is 50 m with uncertainty + 20 % / - 15 % and the length of the LP flame is 15 m +/- 10 % (SINTEF Energiforskning AS, 2006).

To investigate the flames from the simulations, an isosurface of temperature 800 K is plotted for the different cases, as this temperature will represent a visible flame. The view angle of the plots is attempted to be similar to the view angle in the picture showing the real flames. Figure 5.2 shows the *separately* simulated HP and LP flares, combined in *one* picture.

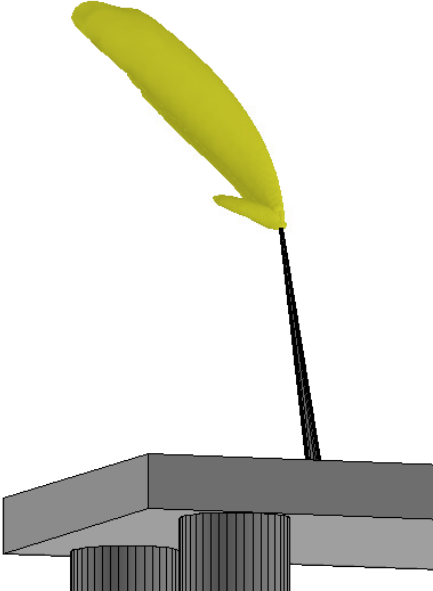
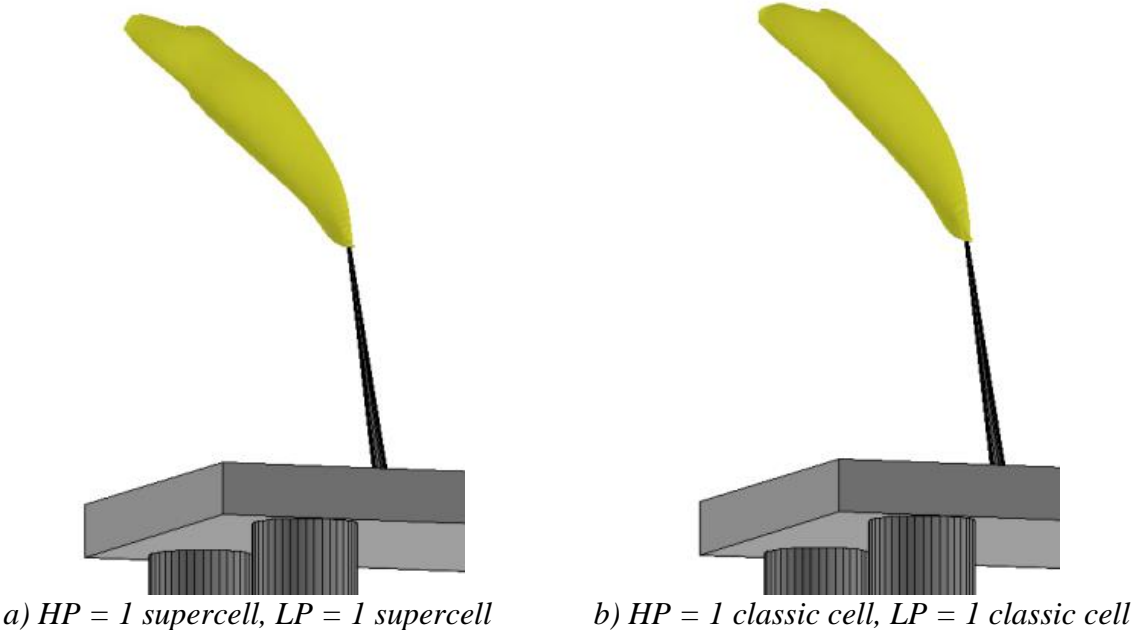


Figure 5.2: Separately simulated HP and LP flare flames combined in one picture

The figure clearly shows that KFX is able to capture the fact that the LP flare flame is located lower than the HP flare flame, when the flares are simulated separately. The simulated lengths of the HP and LP flames is 55 m and 14.5 m respectively, which both are within the uncertainty interval given by SINTEF. Figure 5.3 shows the results when the two flares are simulated *simultaneously*, located at actual locations.



a) HP = 1 supercell, LP = 1 supercell

b) HP = 1 classic cell, LP = 1 classic cell

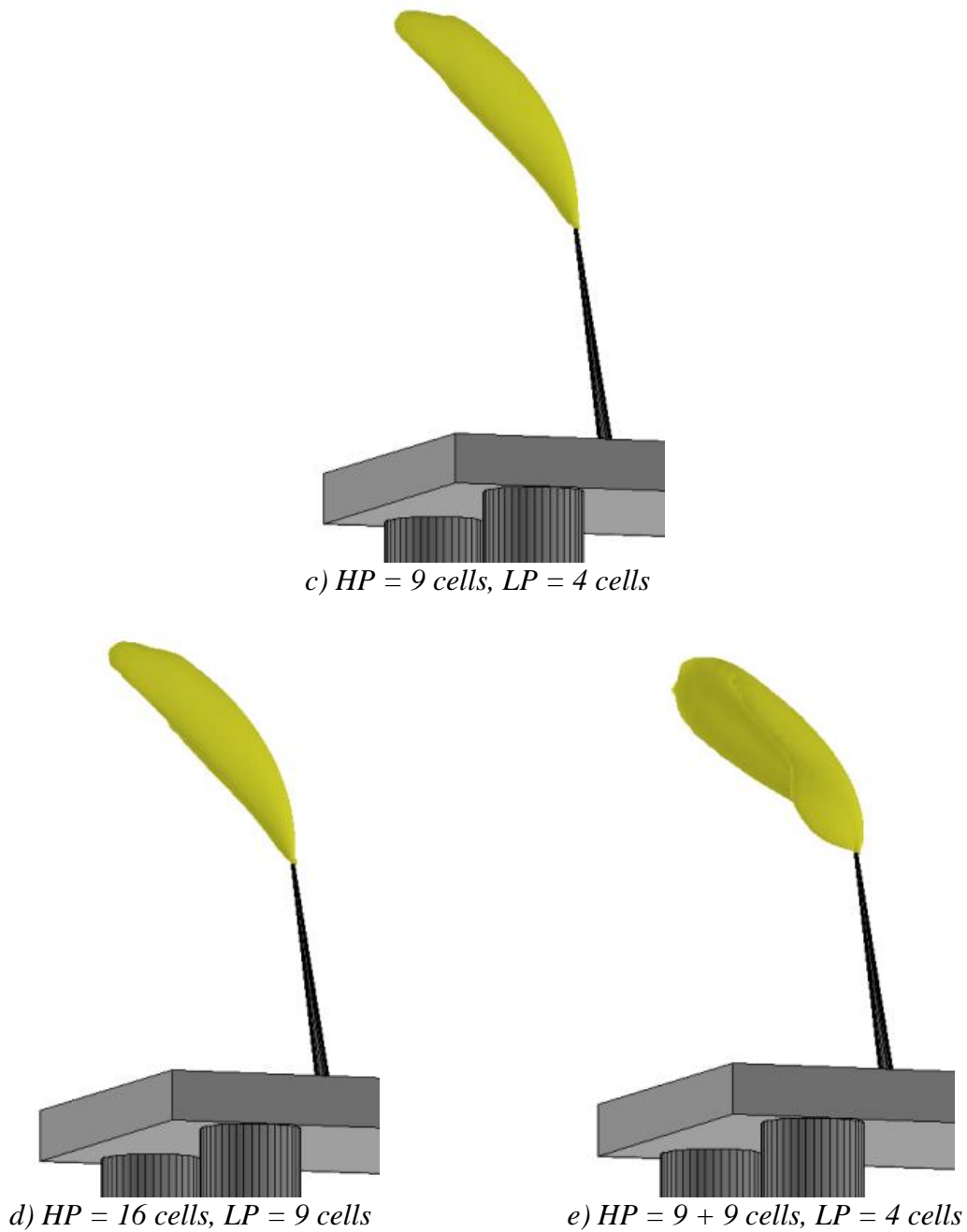


Figure 5.3: Flames when HP and LP flare are simulated simultaneously, at actual locations

As seen in the figure, none of the cases were able to capture the fact that the two flames are separated. Other temperatures than 800 K has also been investigated leading to the same result. The flame in the special case using 9 + 9 cells for the HP flare stands out by being wider than the other flames. This is also the where a contour resembling the LP flame is showing. The two cases run with adjusted location of the LP flare resulted in the following flames:

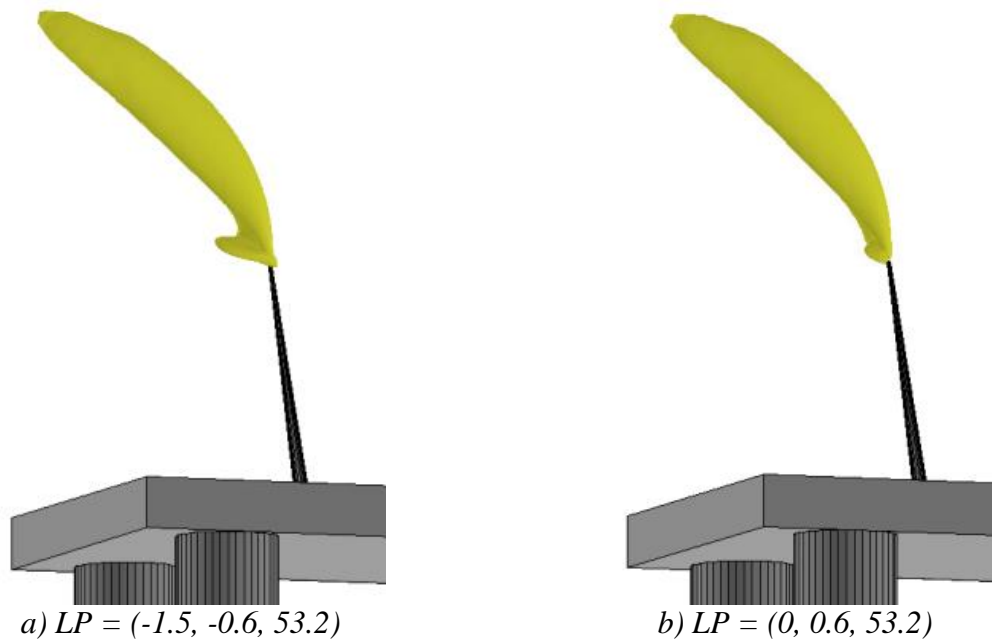


Figure 5.4: Flames with adjusted LP flare locations

When moving the LP flare further away in x-direction, as in $LP = (-1.5, -0.6, 53.2)$ it is seen in a) that this distance actually is enough to clearly see the separation effect. The tip with location $LP = (0, 0.6, 53.2)$ is not moved further away from the HP flare compared to actual locations, it is just moved downstream the HP flare relative to the wind. The LP flame is therefore not blown into the HP flame. It is seen from Figure 5.4 b) that this is not sufficient to capture the separation effect even though an incipient lump is showing. It appears like there has to be at least 5 control volumes between the HP and LP flare to capture the separation effect. Keeping actual locations, refining the grid to a level where there is 5 control volumes between the two flares would result in an unacceptable long simulation time. Since the focus of this study is radiation modeling, trying to obtain the flame separation effect is not pursued further.

5.2 Radiation Levels

Table 5.1 is listing the radiation levels measured by SINTEF at the 6 different measuring locations.

Table 5.1: Measured radiation levels (SINTEF Energiforskning AS, 2006)

Measuring point #	Measured value (kW/m^2)
1	2.76
2	3.71
3	2.93
4	1.57
5	2.72
6	1.85

5.2 Radiation Levels

To compare the simulated radiation levels to the measured levels, the results are presented in a column chart. Figure 5.5 and Figure 5.6 shows the radiation levels and deviations at each measuring point of the cases with actual flare locations. The legend indicates what release cell configuration is used, and the first two cases are marked with S and C meaning supercell and classic release cell, respectively.

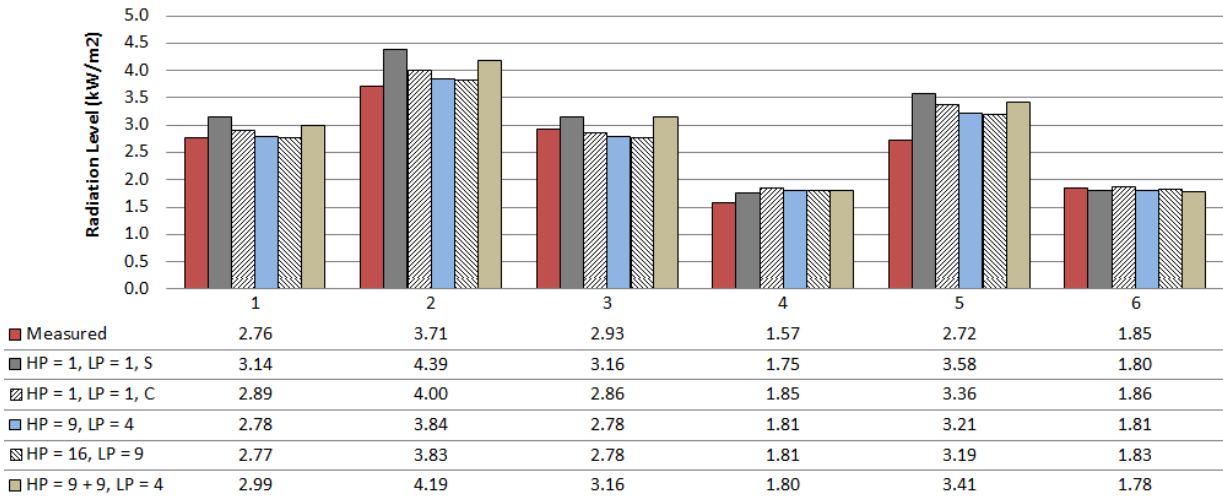


Figure 5.5: Radiation level, actual locations

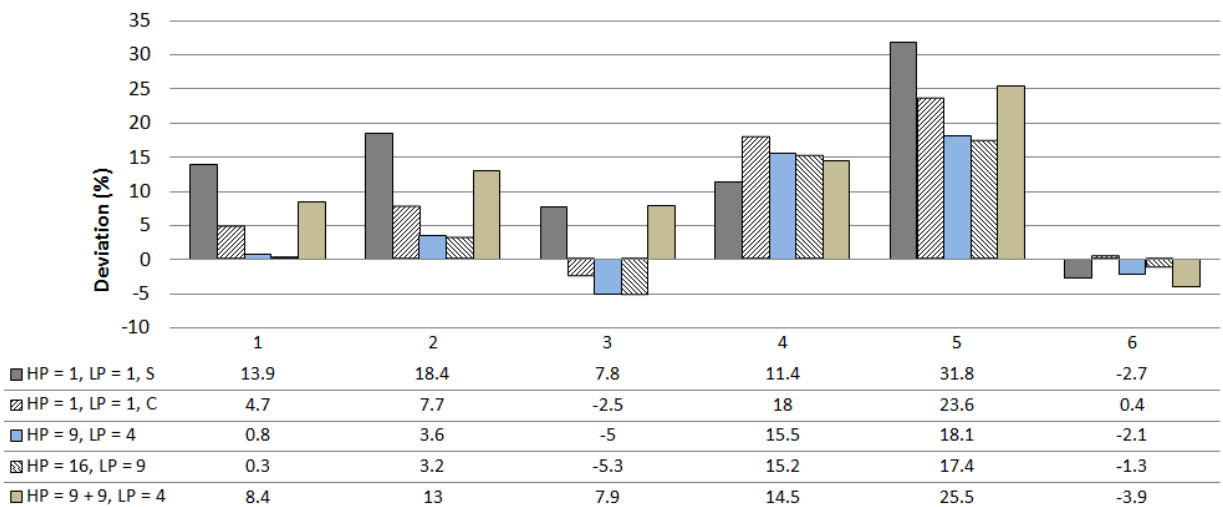


Figure 5.6: Deviation, actual locations

The first interesting result is the comparison between the two cases using only 1 cell for each flare. It was expected that these two cases would have a larger deviation between simulated and measured radiation levels compared to using more cells, but it is surprising that the case using 1 supercell resulted in a much larger deviation than using 1 classic release cell. As the recommended cell type is the supercell, it was expected that the classic release cell would provide a poorer compliance with the measured values, not the other way around. The grid resolution using the classic release cell is also coarser compared to using the supercell. A possible reason for the deviation between the two cell types can be related to how the cell types are optimized. As the supercell is optimized with respect to fires inside modules, and

not flaring scenarios, it can be that the optimization is sacrificing accuracy when modeling inclined flares. Also, when investigating the flames in these two cases more closely, it is seen that the flame when using 1 supercell is slightly larger than using the classic release cell. This small increase might be enough to cause higher radiation levels. As the two different cells are treating the entrainment of air differently, deviations naturally follow, even though the deviation was unexpectedly large. Note that all cases using more than 1 cell are built up by classic release cells.

It is seen in the charts that using 9 and 16 cells for the HP flare together with 4 and 9 cells for the LP flare gives very similar results. This is in accordance with what was discovered in the release cell sensitivity test, described in chapter 3.3.1. These two configurations are also the ones with smallest deviation compared to the measured values. As these are the cases with the finest grid refinement, it was assumed that they would have the lowest deviation, but being almost 0 at measuring point 1 and 6 exceeded the expectations. The special case, with 9 + 9 cells for HP flare and 4 cells for LP flare gives a deviation between the two cases using only 1 cell for each of the HP and LP flare. The coarseness of this grid is closer to the coarseness of using 9 cells for the HP flare and 4 for the LP than using only 1 cell. As the flame in this case was very wide compared to the other cases, this might cause a higher radiation level, leading to the large deviation.

Measuring point number 4 and 5 stands out by having the largest deviation in all cases. A possible reason for why the measured radiation level in measuring point 4 is lower than the simulated level in KFX is related to how the flare stack is modeled. In KFX the stack is quite thin, to avoid shielding effects on the deck. In reality, the stack might be equipped with shielding constructions, e.g. the access platform seen in Figure 5.1, but this is not taken into account in KFX because of lack of details. As measuring point number 4 is located behind the flare stack, relative to where the flare flame is positioned, it might be larger shielding effects from the stack in reality than in the simulations, resulting in lower measured levels compared to simulated levels. The reason for the high deviation in measuring point number 5 is more uncertain. There is no obvious reason that stands out as a possible source of error, and the deviation may be caused by a number of minor error sources. These are all discussed in chapter 5.4.

5.2 Radiation Levels

Figure 5.7 and Figure 5.8 shows the results of the two cases with adjusted LP flare locations.

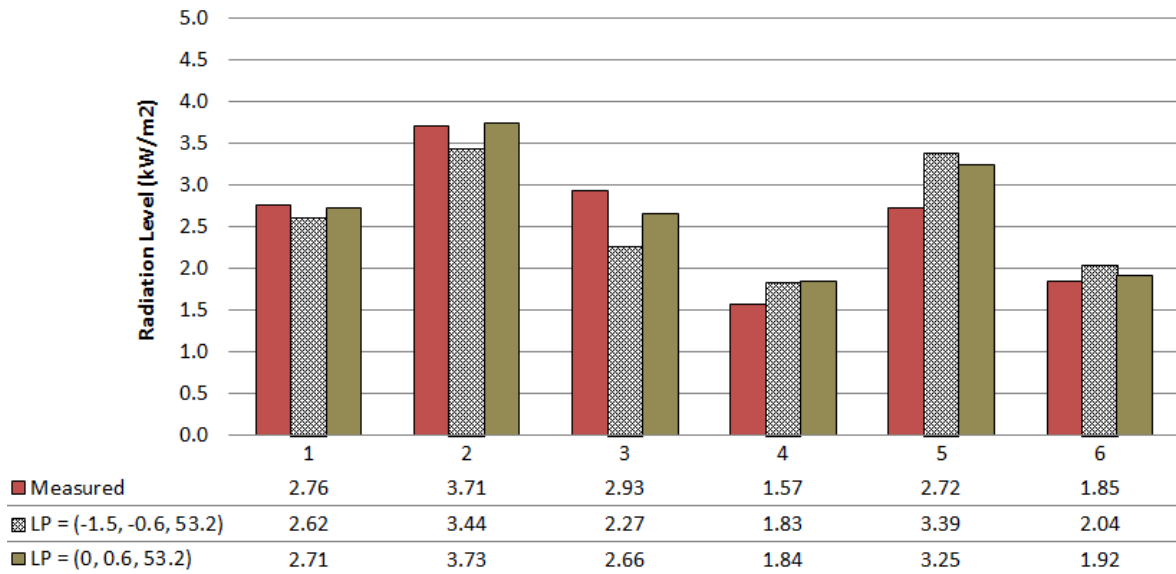


Figure 5.7: Radiation levels, adjusted locations

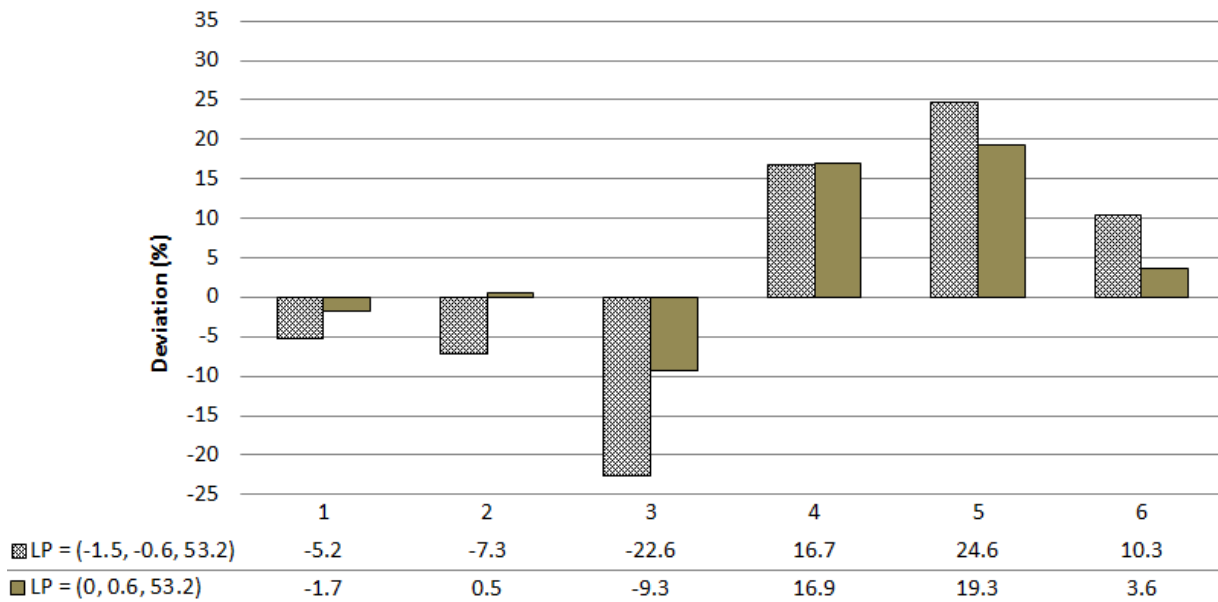


Figure 5.8: Deviation, adjusted locations

The release cells in these two cases have the exact same configuration as the case where the HP flare consist of 9 classic release cells and the LP flare consist of 4. It is seen that moving the LP flare leads to higher deviation between measured and simulated radiation levels. As the location of the LP flare is no longer in accordance with reality, a larger deviation is expected, but with the largest deviation being 24.6% it is still considered to be in relative good compliance with measured levels.

5.3 Simulation Time

It has been emphasized in this thesis that the simulation time is an important aspect when using CFD. Table 5.2 shows the simulation time for the simulated cases with actual locations of the flares, having 1.6 million control volume cells in the domain.

Table 5.2: Simulation time

Case #	# of HP flare cells	# of LP flare cells	Cell type	Time (hours)
1	1	-	Supercell	19
2	-	1	Supercell	2
3	1	1	Supercell	30
4	1	1	Classic release cell	16
5	9	4	Classic release cell	45
6	16	9	Classic release cell	68
Special	9 + 9	4	Classic release cell	127

It is seen that using 1 supercell for each of the HP and LP flares takes twice as long time compared to using 1 classic release cell. For the other cases, the simulation time is increasing with increased number of release cells, which was expected. The special case took inexpedient long time to run, compared to all other cases.

5.3.1 Number of Control Volume Cells

The reason for choosing 1.6 million control volume cells in the simulations in this thesis is based on the analysis conducted in the specialization project that this thesis is a continuation of (Bjørnæs, 2015). It was desired to start with a high number of control volume cells, and focus on release cell modeling before trying to reduce the total number of cells in the domain. In this thesis, no geometry on the deck has to be resolved, and this allows for a very coarse grid far away from the flare flame. If there was any geometry other than the flare stack or the stack was higher etc., it is assumed that at least 1.6 million cells are needed.

The simulation time can be reduced by decreasing the number of cells, and a sensitivity test has been performed on this matter. The chosen case is the one using 9 classic release cells for the HP flare and 4 for the LP flare. Radiation levels have been plotted at the upper deck along three different y -axes; $y = -20$, $y = 0$ and $y = 20$, as shown in Figure 5.9.

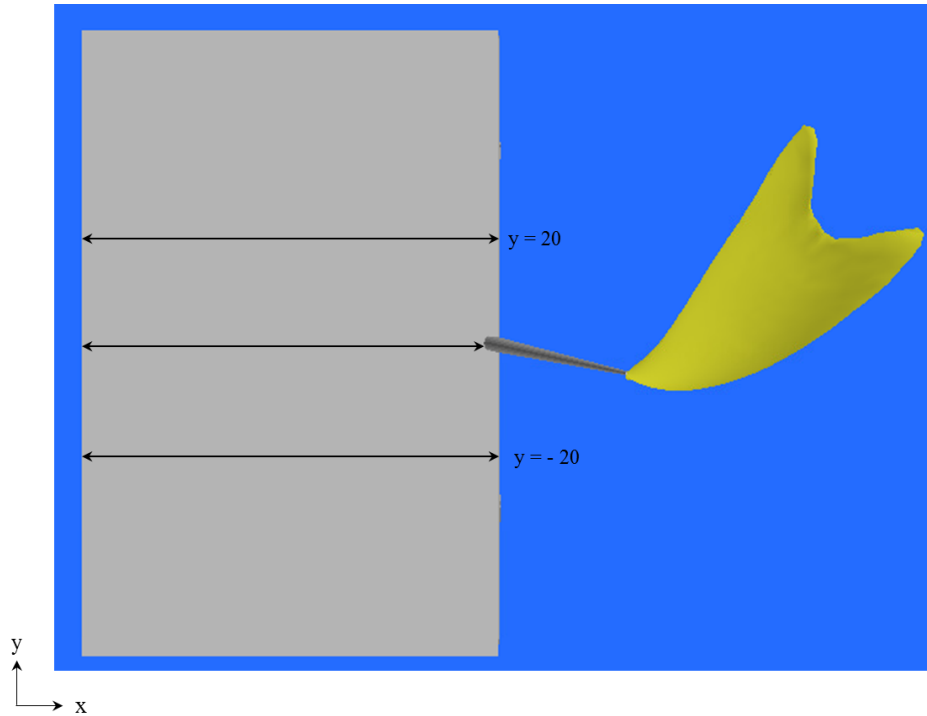


Figure 5.9: Locations for radiation level plots with reduced number of CV cells

The number of control volume cells has been reduced two times, to 1 million cells and 0.7 million cells. Figure 5.10 shows the resulting radiation levels for the three different configurations, where the legend indicates the number of control volume cells given in millions.

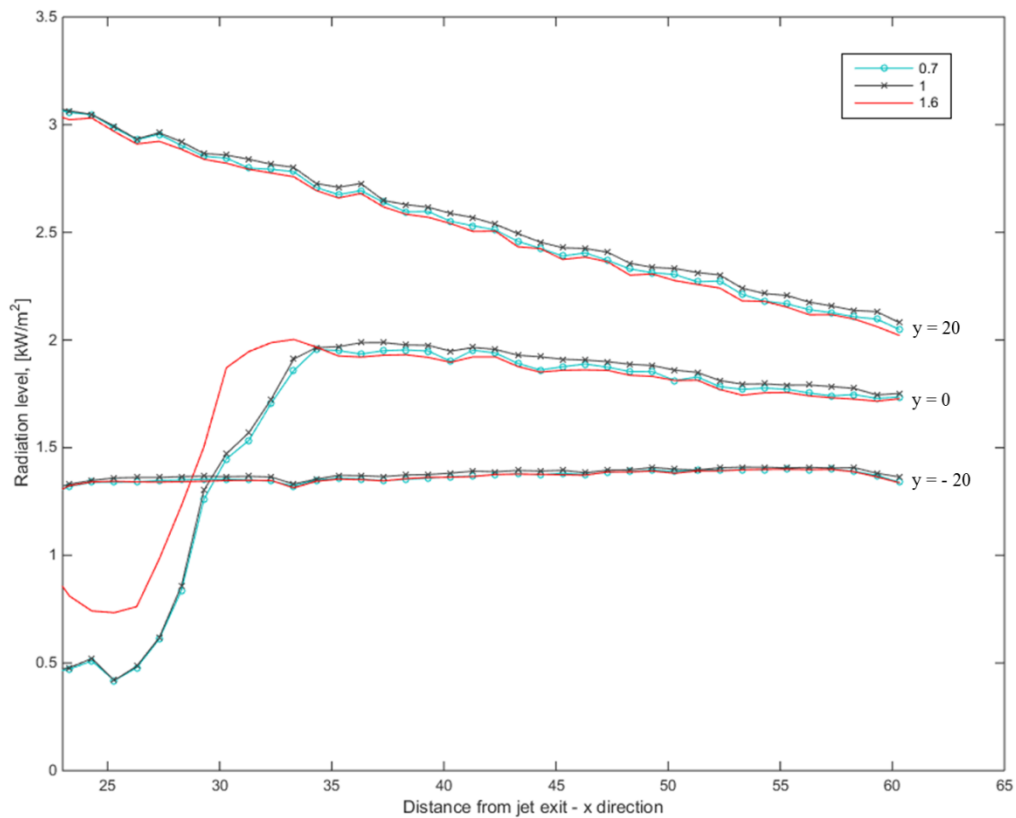


Figure 5.10: Radiation level comparison when reducing the number of CV cells

It is seen that reducing the number of control volume cells does not impact the resulting radiation levels along $y = -20$ and $y = 20$. In the centerline, $y = 0$, on the other hand, a characteristic dip is shown, and there is also a deviation between 1.6 million cells in one side and 0.7 and 1 million on the other. The dip is caused by shielding effects from the stack. The reason for the deviation is related to how the stack is modeled when the number of control volume cells is reduced. As fewer cells are present in the domain, the stack is built up by larger cells causing it to appear bigger than it really is. This results in larger shielding effects and hence lower radiation levels. This is a good example of the effect fewer cells exerts on geometry, and it is clear that if any geometry on the deck were to be resolved, it would be necessary to use more cells. None of the 6 measuring points are affected by this phenomenon, and the radiation levels are close to identical in the three cases for all measuring points, as seen in Figure 5.11.

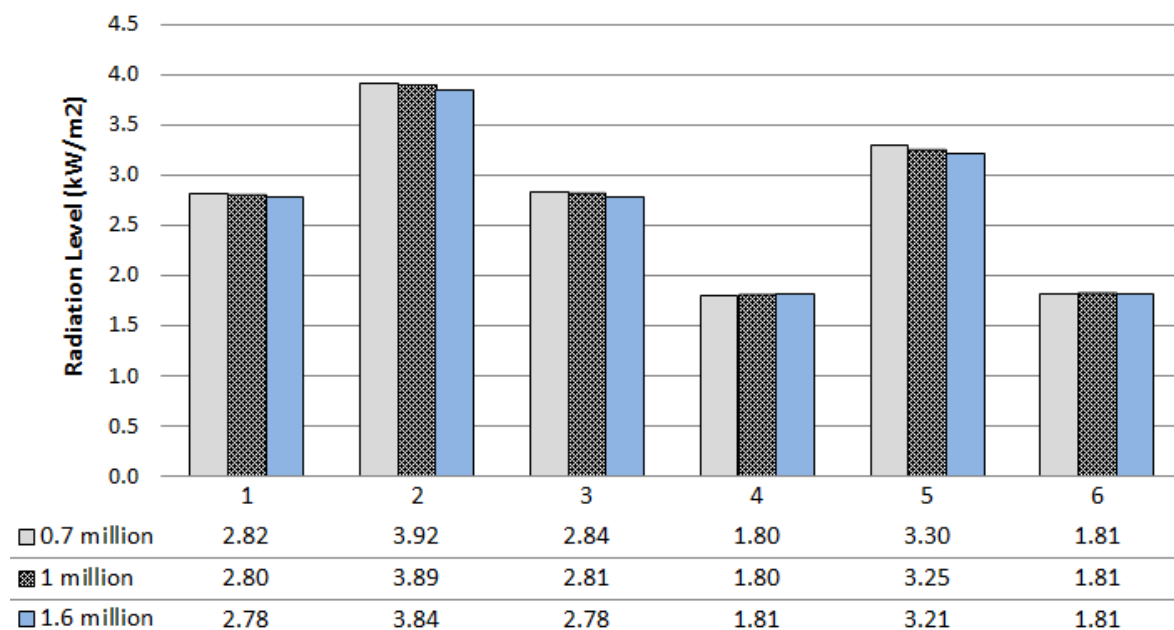


Figure 5.11: Radiation level comparison when reducing the number of cells

As expected, the simulation time is greatly reduced when reducing the number of control volume cells. The result is shown in Table 5.3, and the time when using 0.7 million cells is lower than a third of the time when using 1.6 million cells.

Table 5.3: Simulation time when reducing the number of cells

# of CV cells (mill.)	Time (hours)
0.7	13
1	22
1.6	45

5.4 Discussion

Even though the simulated flare flames did not coincide with the real flames, the deviations between measured radiation levels and simulated levels are generally very small. For all cases the deviation lies between -5 % and +18 % at all measuring points, except measuring point number 5. It does not seem like the fact that KFX did not fully resolve the separation effect between the flames had a large impact on the resulting radiation levels. However, a discussion of factors that may have impact on the deviations will now follow.

Fuel gas composition: As stated in the presentation of parameter values, the fuel gas compositions was not given in the report from SINTEF. Approximated values are therefore used in the simulations, in compliance with the given molecular weight and lower heating value. How the selected composition affect the radiation levels are not known, but are considered to be a minor source of error.

Mass flow of fuel gas: The fuel gas mass flow of the HP and LP flare has been given by SINTEF to be 45.3 and 2.8 kg/s, respectively. These are the values used in the simulations. However, these values are calculated based on pressure drop over the flare tips. It is not given how large the uncertainty interval of the calculations is, it is only stated that the values are estimated with a high degree of certainty.

Wind: The wind direction used in the simulations is set to 210° from North. This is the given direction that is assumed to be correct when the measurements were taken. However, it is stated in the report from SINTEF that the wind was varying in the interval 210 to 220° during the whole test. The actual wind direction is therefore a source of uncertainty. Also, the convective cooling effect the wind exerts on the radiation flux gauges is not known.

Gauge orientation: When setting the view angle of the radiation flux gauges, it is important that they point towards the flame centroid to obtain a high degree of accuracy. The gauges were during measurements pointed towards a calculated flame centroid of the HP flare flame, and there is uncertainty connected to the accuracy of this orientation. The gauges were not adjusted after the flare was lit. It is stated in the report that this will have an insignificant impact on the radiation result.

The total effect of these minor sources of error will naturally cause deviations between the calculated radiation levels and the measured levels to various extents. Overall the deviations between measured and simulated radiation levels are however within an acceptable range.

6 Conclusion

The objective of this thesis was to determine an optimal approach of modeling thermal radiation from a flaring scenario in KFX. Concluding that an approach is *optimal* depends on the desired level of accuracy. Measured radiation levels from a real flaring scenario consisting of two pipe-flares have been used as reference and different modeling approaches resulted in different degrees of deviation. The main workload when using KFX is defining the scenario by choosing input parameters and grid configuration, and trying to replicate exact conditions as during the measurements has been attempted. While keeping the carefully selected input parameters constant, different approaches related to grid configuration and refinement have been investigated to obtain a solution as accurate as possible.

The radiation level results obtained from the simulations in KFX correspond well with the measured levels. It is a clear connection between the refinement of the grid and accuracy. The finest grid resulted consistently in the lowest deviation for all measuring points. The largest deviation was found in the case where 1 supercell was used to represent each of the two flares. If a rough estimate of radiation level is desired, 1 cell can be used, but according to the results of the cases simulated in this thesis the classic release cell should be chosen over the supercell. A special case tried in this thesis, building the HP flare up by two planes, instead of regular subdivision of cells, did not result in any smaller deviation. Also, the flare flame in this case looked quite unrealistic and the simulation time was very long, so this approach is not recommended. As the two cases using 9 and 16 cells for the HP flare provided almost equal radiation levels, 9 cells should be the preferred choice as this took half the time to run. To reduce the simulation time even further, the number of control volumes could in this case be reduced without affecting the resulting radiation levels.

The approach concluded optimal in this thesis is applicable for the specific scenario simulated here. To the general case, it is not necessarily 9 cells that is the best choice regardless of the flare properties. However, in general it can be concluded that the accuracy of the simulated radiation levels will depend on the refinement of the release cells. Many small cells give better accuracy compared to few big cells. Conducting a release cell sensitivity test is recommended as a necessary procedure regardless of flaring scenario, to improve accuracy.

6.1 Further Work

The reason for simulating a flare system built up by two pipe-flares in this thesis is related to the availability of measured radiation levels. If a flare having a multiple nozzle tip were to be simulated, even higher requirements of grid refinement would possibly apply. This has not been investigated due to the lack of measured values with accompanying ambient conditions. Simulating a flare system containing a multiple nozzle flare could therefore be subject to further work.

References

- American Petroleum Institute. (2007). API RP 521 *Pressure-relieving and Depressuring Systems*: 5th edition.
- Anderson, J. D. (2007). *Fundamentals of Aerodynamics* (4th ed.): The McGraw Hill.
- Barratt, R. (2013). *Atmospheric Dispersion Modelling: An Introduction to Practical Applications*: Taylor & Francis.
- Baukal, C. E. (2000). *Heat Transfer in Industrial Combustion*: CRC Press.
- Baukal, C. E. (2013). Safety *The John Zink Hamworthy Combustion Handbook: Design and Operations* (2nd ed., Vol. 2, pp. 1 - 44): CRC Press.
- Birch, A. D., Hughes, D. J., & Swaffield, F. (1987). Velocity Decay of High Pressure Jets. *Combustion Science and Technology*, 52(1-3), 161-171.
- Bjørnæs, M. (2015). *Study of radiation hazard from ignited flares at process plants*. Project work. NTNU.
- Brzustowski, T. A., & Sommer, E. C. (1973). Predicting Radiant Heating from Flares *Proceedings - Division of Refining* (Vol. 53, pp. 865 - 893). Washington D.C.: American Petroleum Institute.
- Chamberlain, G. A. (1987). Developments in Design Methods for Predicting Thermal Radiation from Flares *Transactions of the Institution of Chemical Engineers* (Vol. 65, pp. 299 - 309).
- Crist, S., Glass, D. R., & Sherman, P. M. (1966). Study of the Highly Underexpanded Sonic Jet. *AIAA journal*, 4, 68-71.
- Crocker, W. P., & Harper, D. H. (1988). Mathematical Models for the Prediction of Thermal Radiation from Jet Fires *Preventing Major Chemical and Related Process Accidents* (pp. 331-347).
- Cumber, P. S. (1995). Improvements to the Discrete Transfer Method of Calculating Radiative Heat Transfer *International Journal of Heat and Mass Transfer* (Vol. 38, pp. 2251-2258).
- Ertesvåg, I. S. (2000). *Turbulent Strøyming og Forbrenning: frå Turbulensteori til Ingeniørverket*. Trondheim: Tapir akademisk forlag.
- Evanger, T., & Vembe, B. E. (2011). *Frustum User Manual*. (R1132).
- Guigard, S. E., Kindzierski, W. B., & Harper, N. (2000). Heat Radiation from Flares.
- Hottel, H. C., & Sarofim, A. F. (1967). *Radiative Transfer*: McGraw-Hill.
- Incropera, F. P., Dewitt, D. P., Bergman, T. L., & Lavine, A. S. (2013). *Principles of Heat and Mass Transfer* (7th ed.). Hoboken, N.J.: Wiley.

- Jacobson, M. Z. (2005). *Fundamentals of Atmospheric Modeling* (2nd ed.): Cambridge University Press.
- Lockwood, F. C., & Shah, N. G. (1981). A New Radiation Solution Method for Incorporation in General Combustion Prediction Procedures *Symposium (International) on Combustion* (Vol. 18, pp. 1405-1414).
- Modest, M. F. (2003). *Radiative Heat Transfer*: Academic Press.
- Monin, A. S., & Obukhov, A. M. (1954). Basic Laws of Turbulent Mixing in the Surface Layer of the Atmosphere.
- NORSOK. (2008). NORSOK Standard S-001 *Technical Safety*: 4th edition.
- Prema-Service. Retrieved from <http://www.prema-service.com/en/products/flare-systems/flare-heads/>
- Schwartz, R. E., White, J., & Bussman, W. (2013). Flares *The John Zink Hamworthy Combustion Handbook: Applications* (2nd ed., Vol. 3, pp. 251-297): CRC Press.
- SINTEF Energiforskning AS. (2006). *Måling av stråling og støy fra fakkell på (...) juni 2006*. (TRF6399).
- Thermal-FluidsCentral. (2010). Retrieved from https://www.thermalfluidscentral.org/encyclopedia/index.php/Numerical_Solution_of_Flow_Field
- Vembe, B. E., Kleiveland, R. N., Grimsmo, B., Lilleheie, N. I., Rian, K. E., Olsen, R., . . . Evanger, T. (2014). *Kameleon FireEx User Manual*. (R1421).
- Vembe, B. E., Rian, K. E., Holen, J. K., Lilleheie, N. I., Grismo, B., & Myhrvold, T. (2001). *Kameleon FireEx Theory Manual* (R0123).
- Versteeg, H. K., & Malalasekera, W. (2007). *An Introduction to Computational Fluid Dynamics: The Finite Volume Method*: Pearson Education Limited.
- White, F. M. (2011). *Fluid Mechanics* (7th ed.): McGraw Hill.
- White, J., & Bussman, W. (2012). Flare Radiation *The John Zink Hamworthy Combustion Handbook: Fundamentals* (2nd ed., Vol. 1, pp. 207-225): CRC Press.

Appendix A Sensitivity Tests

A.1 Restart Files

When running a simulation in KFX, it is possible to specify a certain time interval for when restart files should be saved. A restart file allows the user to restart the simulation at a specific time, instead of running the whole simulation from start. A problem using these files was discovered early in the simulations performed in this thesis. A sensitivity tests were therefore conducted on the same random case as in the release cell sensitivity test described in chapter 3.3.1, using 1 rectangular supercell with size 0.6332 x 0.6332 x 1.2664 m.

Radiation levels were extracted 100 m underneath the flare tip when the simulated time had reached 90 seconds. A restart file was also saved at 90 seconds. According to common practice, it should then be possible to restart the simulation at 90 seconds, and immediately extract results that would be equal to the ones obtained running the full simulation. This is often done for various reasons. Figure A.1 shows extracted radiation levels at some specified times for the first run of the full simulation.

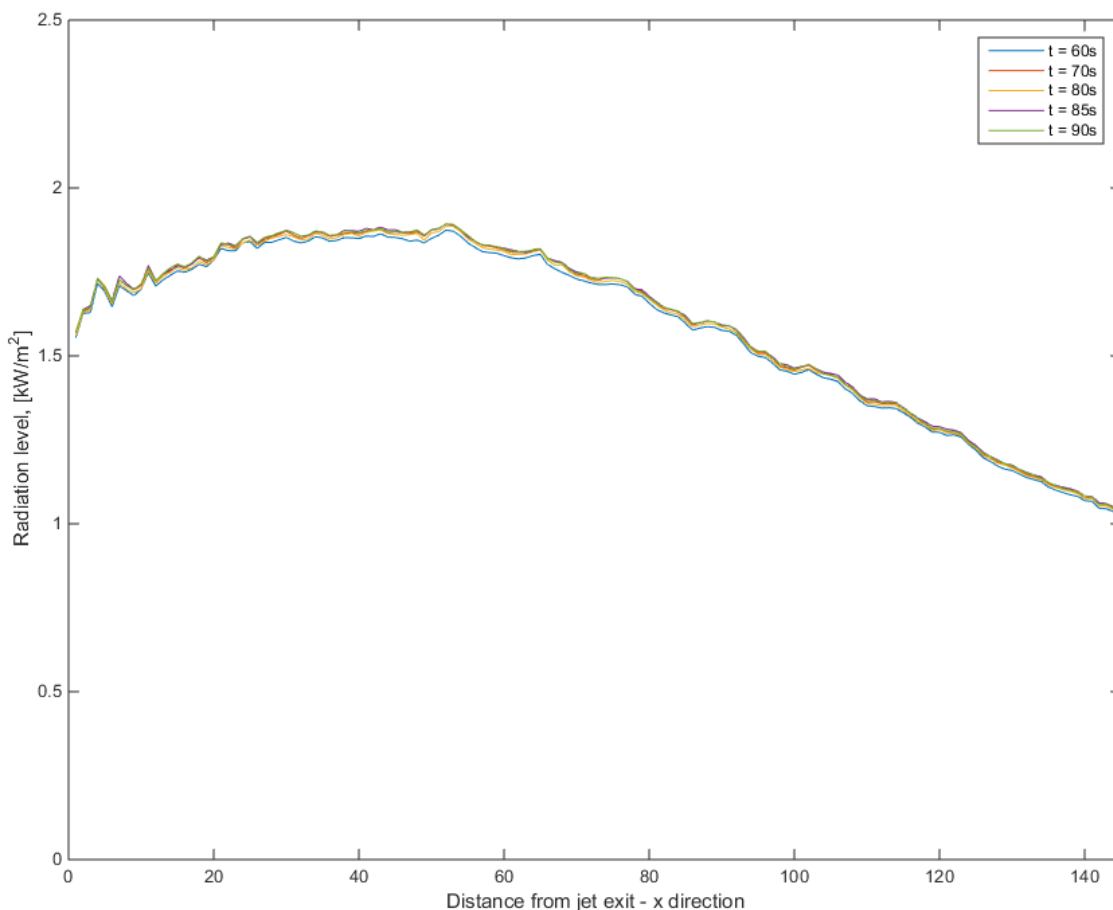


Figure A.1: First run of full simulation

It is clearly seen that the solution has converged, and is constant already from 60 seconds. It was then tested to restart the simulation at 90 seconds, and immediately extract radiation

levels at the same locations, without doing any changes other than restart the simulation. The result is seen in Figure A.2.

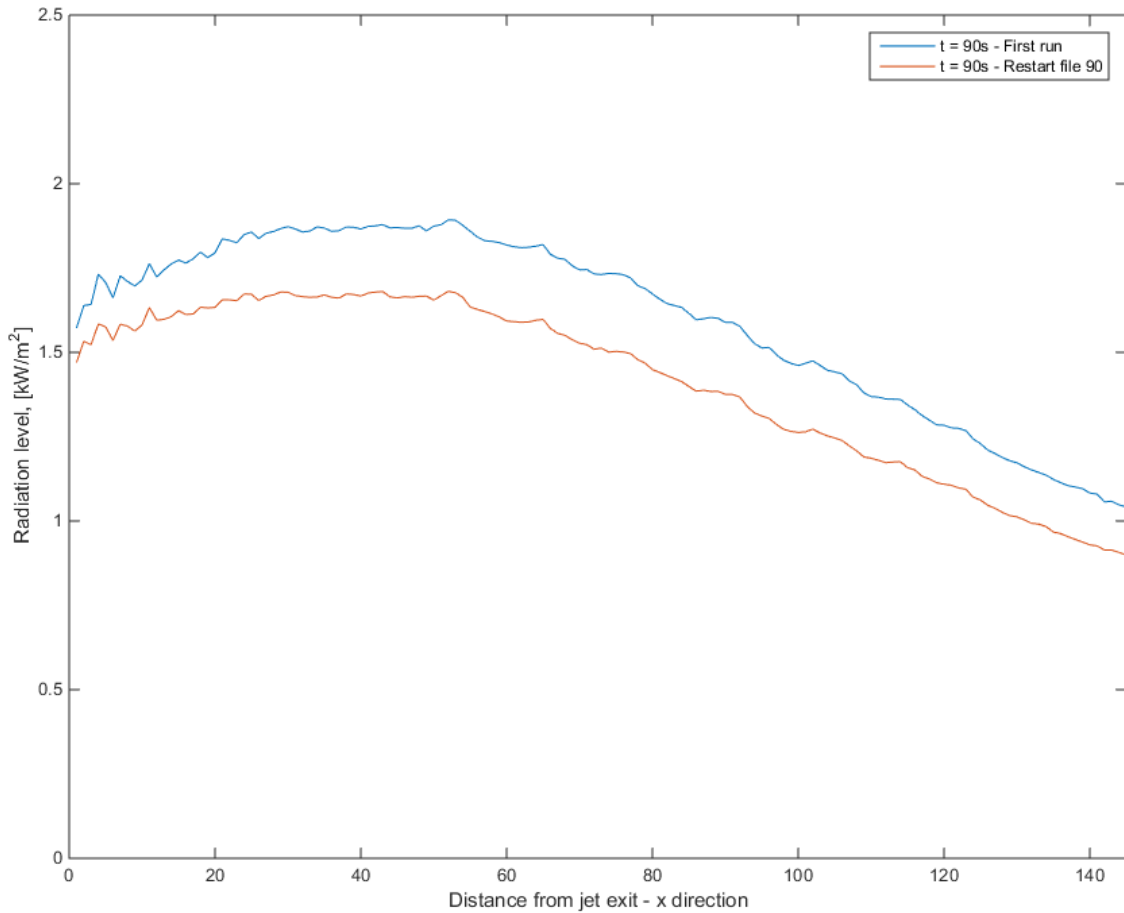


Figure A.2: Results at $t = 90s$ for first run and restarted simulation

The radiation level extracted after restarting the simulation is clearly not the same as when running the full simulation. Further tests were conducted to investigate the problem.

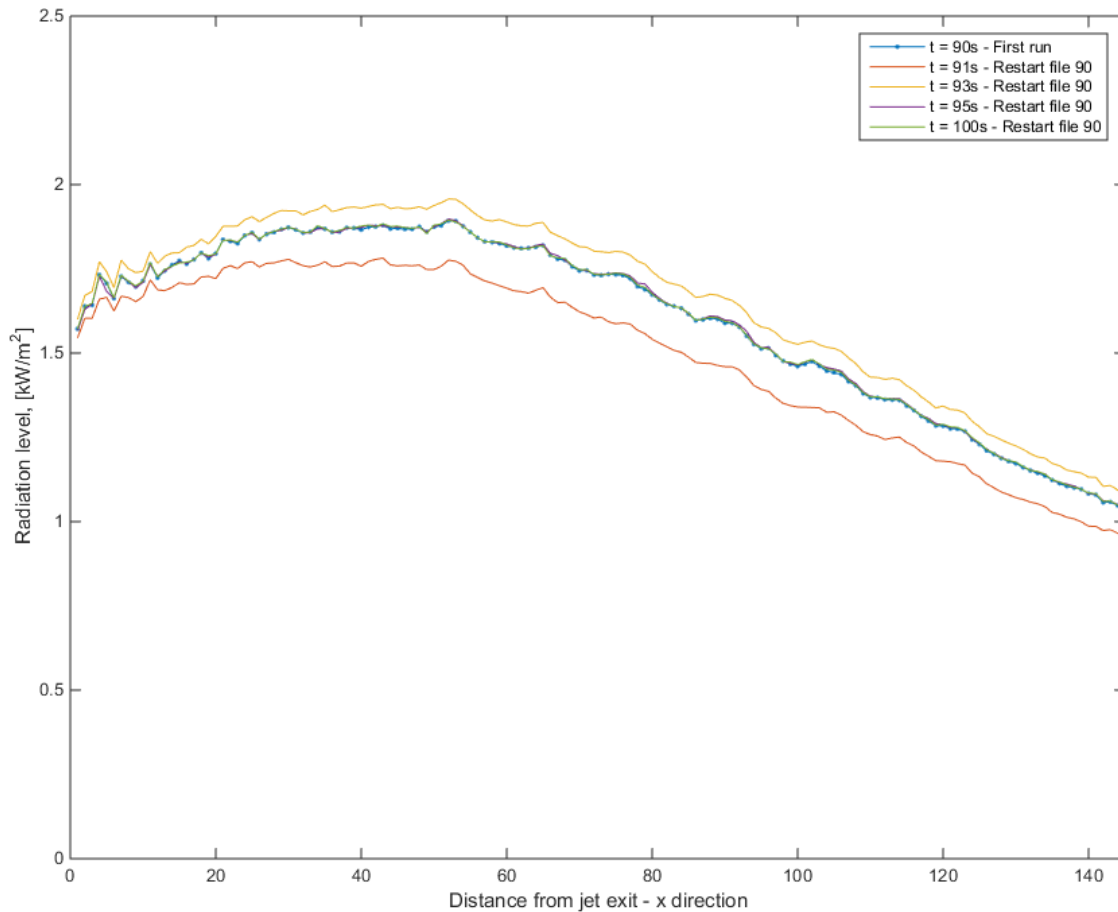


Figure A.3: Results at different times using restart file 90

As seen from Figure A.3 the simulation had to simulate at least 5 seconds more to converge towards the original solution from the first run. At 91 seconds, the solution is lower, at 93 seconds the solution is higher, but at 95 and 100 seconds the solution is the same as in the first run.

The reason for this happening is that when the user restarts the simulation, KFX conducts one iteration before checking if the maximum time is reached. The data from the restart file is the input data for the restarted simulation and once the iterations has started it takes some time before the solution is stabilized again. This is caused by a variable that is not stored in the restart file, and has to be calculated all over again if the iterations start. To avoid the problem, it was discovered that KFX checks if the maximum time step is reached *before* conducting an iteration. If maximum time step is set to 0, before restarting the simulation, KFX will immediately save the stored radiation levels from the restart file, and the same result as in the first run is obtained. This was fortunately discovered early in this thesis.

A.2 Courant Number

As described in chapter 3.1.3, the maximum Courant number criterion determines the size of the time steps used in the simulations in KFX. As ComputITs recommendation for maximum values used in flaring scenarios are in the interval 10 to 20, both these values are tested, to reveal its influence on radiation results. A higher Courant number leads to shorter runtime of the simulations, which is the reason for wanting to keep the number as high as possible. The test was conducted on the same random case as the release cell sensitivity test, using 9 rectangular cells to represent the fuel discharge.

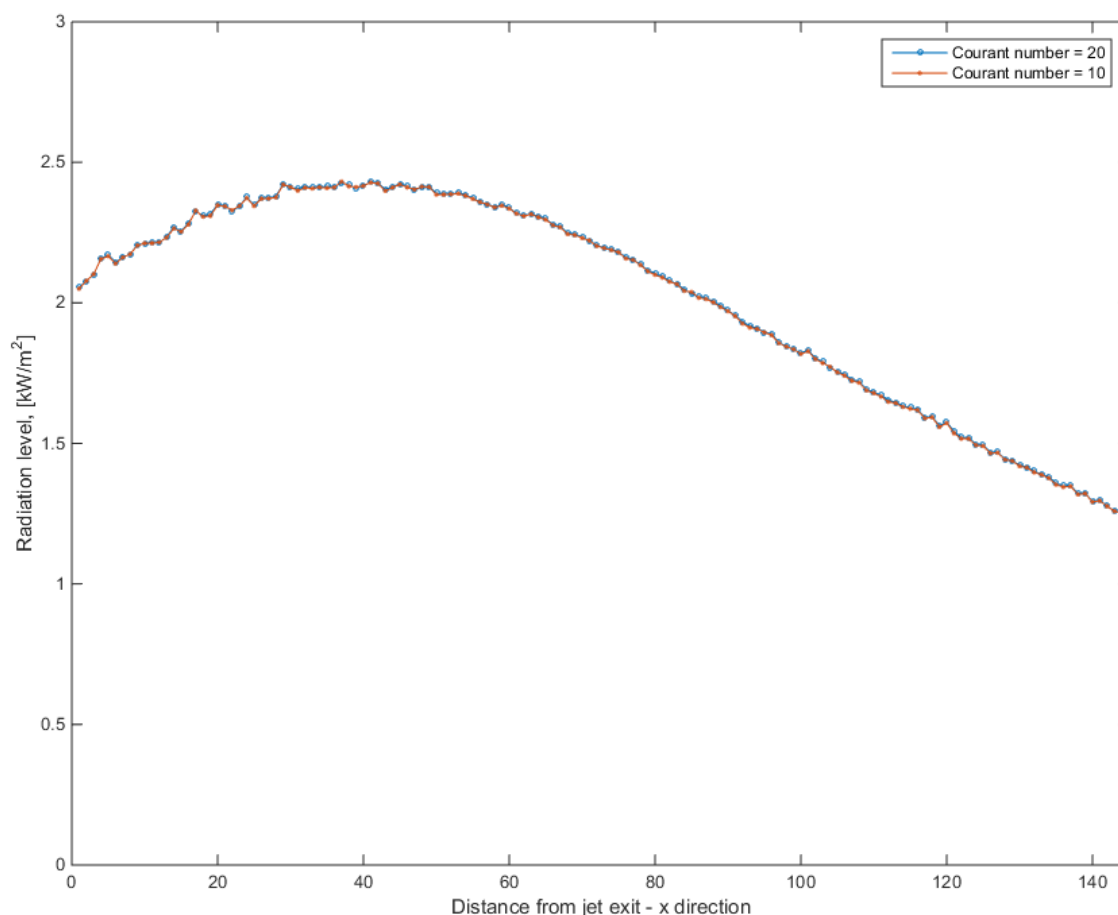


Figure A.4: Results using Courant number 10 and 20

As seen in Figure A.4 the radiation level is not influenced by the choice of Courant number. The simulation with Courant number 20 ran twice as fast as the one using 10. It is concluded from the test that Courant number 20 will be used for the simulations in this thesis.

A.3 Number of Ordinates

In KFX the user must specify where it is desired to calculate the radiative heat flux. It would be very computational intensive to calculate the flux in all free flow cells, since only the intensities of the rays are needed to obtain a solution. There is a special built-in feature in KFX called *bullet monitors* which works by storing intensities on spherical surfaces. These surfaces are discretized in the same way as represented in Figure 3.15 and the fluxes are calculated using vector multiplication. It is important to choose how many ordinates, i.e. the number of solid angles the bullet monitors should be discretized into, to capture enough rays to get an accurate solution

A sensitivity test regarding the number of ordinates has been conducted. In addition to choosing the number of ordinates, it is also possible to enable an *adaptive trace* of the rays. The adaptive trace is a new function in KFX, and it means that fewer ordinates are required to capture the solution than before, as the rays are directed towards the flare flame. The sensitivity test to ensure that a sufficient number of ordinates is chosen has been performed on the same case as above using 9 rectangular release cells. The resulting radiation levels are shown in Figure A.5.

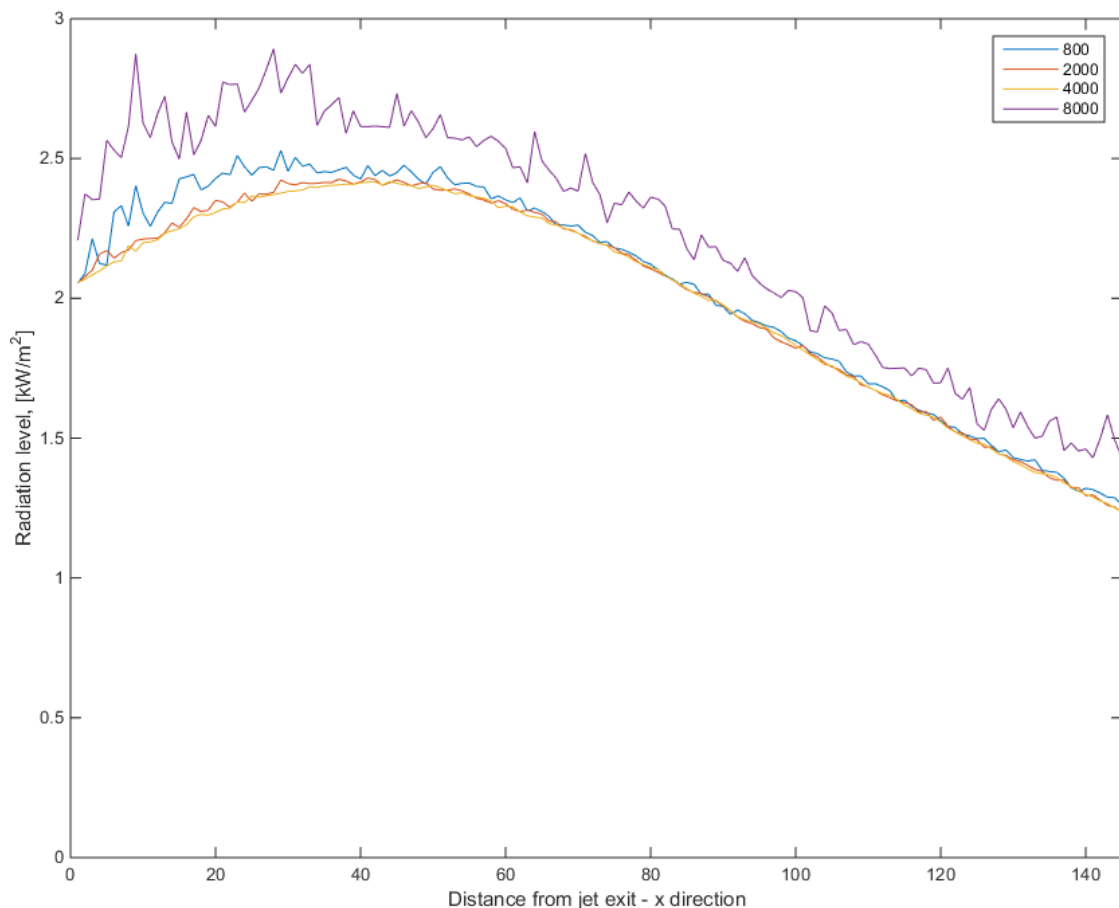


Figure A.5: Result of the sensitivity test of choosing the number of ordinates

When using 800, 2000 and 4000 ordinates, the adaptive trace function were enabled. Using 8000 ordinates the adaptive trace function were disabled. It is a clear distinction

between using 8000 on one side and 800, 2000 and 4000 on the other. It is desirable to have as smooth curves as possible.

The fact that 8000 ordinates predict higher radiation levels than 800, 2000 and 4000 may be caused by the weighing of the rays. When the adaptive trace is disabled, it is random how many rays actually hit the flare flame. The rays that actually hit the flame will then represent a bigger solid angle, and if the rays hit the flame edge, the contribution may be unrealistically high. The conclusion of this test is therefore to use 2000 or 4000 ordinates with adaptive trace enabled as these have the smoothest curves. Since the bullet monitor files require a lot of storage space, and it takes more time to calculate the higher number of ordinates, 2000 is used in the simulations in this thesis. The deviation between 2000 and 4000 is so small that it does not outweigh the space and time needed using 4000 ordinates.